https://doi.org/10.5194/egusphere-2026-1972
Preprint. Discussion started: 14 April 2026
© Author(s) 2026. CC BY 4.0 License.

Modeling thermodynamically consistent phase transitions in multi-component assemblages: An entropy method for geodynamic models

Ranpeng Li[1], Juliane Dannberg[1], Rene Gassmöller[1], and Robert Myhill[2]
[1]GEOMAR Helmholtz Centre for Ocean Research Kiel
[2]University of Bristol
Correspondence: Ranpeng Li (rli@geomar.de)

Abstract.

Phase transitions strongly influence mantle convection as their effects on buoyancy can hinder or accelerate slabs and plumes. In a heterogeneous mantle, different mineral assemblages undergo phase transitions at different depths, leading to lateral buoyancy variations that can cause specific compositions to stagnate or accumulate within characteristic depth ranges. However, complex phase relations, abrupt changes in material properties, and the release and absorption of latent heat pose significant challenges for modeling phase transitions. Our previous work addressed these challenges by formulating the energy equation in terms of entropy rather than temperature, but remained limited to chemically homogeneous models.

Here we extend the entropy formulation to multiple components. By solving one entropy advection equation for each chemical component and then thermally equilibrating all components, our method enables a thermodynamically consistent treatment of phase transitions in multi-component systems. Our tests demonstrate that the method accurately conserves energy, and remains robust even for degenerate cases. We show its applicability in a series of global convection models, which reveal that small differences in phase relations between a pyrolitic equilibrium assemblage and a basalt–harzburgite mechanical mixture with the same composition can lead to major differences in convection patterns. Our results highlight the importance of accurately capturing the full effects of phase transitions in a chemically heterogeneous mantle, and our approach enables new investigations into how planetary interiors evolve.

1 Introduction

1.1 Phase transitions in a heterogeneous mantle

Solid-state phase transitions play a key role in Earth's dynamic evolution and in shaping mantle heterogeneity. They impact flow through changes in buoyancy according to their Clapeyron slope and density contrast between phases and affect the mantle temperature through release or consumption of latent heat. Endothermic phase transitions, which are characterized by negative effective thermal expansivity during the transformation, generate forces that counteract both upwelling and downwelling flow. For example, the formation of bridgmanite and ferropericlase from ringwoodite at around 660 km depth has been shown to

https://doi.org/10.5194/egusphere-2026-1972
Preprint. Discussion started: 14 April 2026
© Author(s) 2026. CC BY 4.0 License.

temporarily stagnate slabs (Fukao and Obayashi, 2013; Agrusta et al., 2018; Arredondo and Billen, 2017). Exothermic phase transitions have the opposite effect and can accelerate mantle flow. While the major phase transitions of Earth's average mantle composition have been known for a long time (Faccenda and Dal Zilio, 2017), it has also been recognized that chemical heterogeneity can significantly alter the equilibrium mineral assemblages in mantle material (Xu et al., 2008). Since the chemical composition of slabs, plumes, and other parts of the mantle can differ significantly from an average mantle composition, they undergo different phase transitions, with implications for their dynamics and thermal evolution. This behavior must be accurately incorporated into models to address key questions about Earth's deep interior. In particular, what role do phase transitions play in Earth's thermal and chemical evolution, and how do they affect mantle structure and heterogeneity? How do compositional differences in phase relations influence mantle flow, such as the subduction of basaltic crust together with harzburgitic lithosphere and the entrainment of various chemical components in mantle plumes? Which phase relations dominate the present-day Earth for typical and atypical mantle compositions and how do they control the distribution of chemical heterogeneity and the resulting seismic observables?

The importance of accurately representing phase assemblages for different chemical components can be illustrated through the life cycle of oceanic plates. The basaltic crust formed at mid-ocean ridges (and the underlying harzburgitic lithosphere) is less dense than the underlying sublithospheric mantle composition and therefore contributes positive buoyancy to the subducting plate at shallow depth. In the upper mantle, the basaltic crust becomes denser than the surrounding pyrolitic mantle after its eclogitization at a depth around 50 km (Billen, 2008), and it remains denser over most of the mantle depth range down to the core-mantle boundary. As a result, basaltic material may accumulate near the base of the mantle and remain there over long periods of time, only being disrupted or entrained during interactions with rising mantle plumes (Koppers et al., 2021; Mulyukova et al., 2015; Nakagawa et al., 2010). A reversal of this density contrast occurs between 660 and 740 km depth (for mantle material with a potential temperature of around 1600 K), where the depth difference between the ringwoodite $\leftrightarrow$ bridgmanite + ferropericlase transition in pyrolite and the post-garnet transition in basalt temporarily renders the basaltic component less dense than the surrounding mantle (Irifune and Ringwood, 1993; Hirose et al., 1999). Consequently, basalt might also accumulate near the base of the transition zone (Yan et al., 2020; Goes et al., 2022). Chemical heterogeneities can also affect the stability and location of plume upwellings (Davaille et al., 2003; McNamara and Zhong, 2004; Torsvik et al., 2006) as well as plume morphology (Dannberg and Sobolev, 2015; Lin and van Keken, 2006). On both the local and the global scale, including multiple chemical components in dynamic models can lead to different structural evolution and convective styles (Xu et al., 2008; Goes et al., 2022).

1.2 Challenges in modeling phase transitions

Phase transitions have been incorporated into geodynamic models in a variety of ways over the last few decades. Early numerical modeling studies implemented phase transformations through analytical phase functions (e.g., hyperbolic tangent or step functions), which describe the proportion of stable phases as a function of depth (Christensen and Yuen, 1985; Peltier and Solheim, 1992). Although easy to implement, such parametrizations are significant simplifications of the equation of state for mantle rocks (Connolly, 2009; Stixrude and Lithgow-Bertelloni, 2011). Because mantle materials are multiphase assemblages

https://doi.org/10.5194/egusphere-2026-1972
Preprint. Discussion started: 14 April 2026
© Author(s) 2026. CC BY 4.0 License.

involving several minerals with extensive solid solutions, their thermodynamic properties are affected by nonlinear interactions between mineral components and cannot be well represented by simple parameterizations in pressure–temperature space. Phase diagrams of natural rocks contain multiple intersecting phase boundaries featuring non-constant Clapeyron slopes, and include assemblages that are only stable over narrow pressure–temperature ranges (Stixrude and Lithgow-Bertelloni, 2022; Dong et al., 2025). Phase functions can only consider a limited number of phase relations and generally extend throughout the whole temperature range with a fixed Clapeyron slope. Another challenge comes from including latent heat of very thin phase transitions numerically, which depends on accurately computing the effective thermal expansivity and specific heat as derivatives of the thermodynamic potential (Christensen and Yuen, 1985).

Advances in thermodynamic modeling and mineral physics databases (Connolly, 2009; Stixrude and Lithgow-Bertelloni, 2011, 2022) have enabled the use of pre-computed thermodynamic lookup tables indexed by pressure and temperature (Nakagawa et al., 2009; Gerya et al., 2004). Phase transitions are naturally incorporated as the state changes, and the method efficiently handles multiple complex transitions. However, some mantle phase transitions (for example, the ringwoodite $\leftrightarrow$ bridgmanite + ferropericlase transition near 660 km) are extremely thin and involve abrupt changes in thermodynamic properties, such as density and enthalpy. The resulting spikes in effective thermal expansivity and specific heat make the calculations of latent heat that is required for geodynamic simulations mathematically ill-posed. Yet smoothing these spikes would alter their dynamic effect: The sharper an endothermic phase transition, the more it impedes flow and promotes layering of convection (Christensen and Yuen, 1985; Tackley, 1995; Dannberg et al., 2022). In a previous paper (Dannberg et al., 2022), we introduced an alternative method that solves the energy equation for entropy rather than for temperature and correspondingly relies on pressure–entropy lookup tables, rather than pressure-temperature tables. This approach overcomes the challenges described above, enabling robust thermodynamic–geodynamic coupling and allowing accurate geodynamic simulations incorporating extremely sharp phase transitions with realistic thermodynamic properties and dynamic effects. However, a key limitation of this method is its assumption of an isochemical mantle.

We here extend our entropy-based formulation of the energy equation to allow multiple compositionally-distinct components. In Section 2.2, we discuss the governing equations and the physical assumptions and processes involved. Section 3 describes the numerical implementation and the requirements for lookup tables used in our method. In Section 4, we present a series of benchmark cases to demonstrate the correctness and consistency of our method. In Section 5, we present two series of global convection models that illustrate how differences in phase transitions between mineral assemblages can affect mantle convection, highlighting the potential of our method to gain new insights in mantle dynamics and evolution. The paper concludes with a summary of our findings.

https://doi.org/10.5194/egusphere-2026-1972
Preprint. Discussion started: 14 April 2026
© Author(s) 2026. CC BY 4.0 License.

2 Governing equations

Geodynamic models of the solid Earth are governed by momentum, mass, and energy conservation in a slowly deforming, compressible, viscous fluid. The system is often described by the following set of equations:

$$-\nabla \cdot (2\eta\dot{\varepsilon}) + \nabla P = \rho \mathbf{g}, \tag{1}$$

$$\frac{\partial \rho}{\partial t} + \nabla \cdot (\rho \mathbf{u}) = 0, \tag{2}$$

$$\rho C_P \left(\frac{\partial T}{\partial t} + \mathbf{u} \cdot \nabla T \right) - \nabla \cdot (k \nabla T) = \rho Q + 2\eta\dot{\varepsilon} : \dot{\varepsilon} + \alpha T \left(\frac{\partial p}{\partial t} + \mathbf{u} \cdot \nabla p \right) \tag{3}$$

where $\mathbf{u}$ is the velocity, P is the pressure, ρ is the density, $\mathbf{g}$ is the gravity vector, η is the viscosity, and $\dot{\varepsilon}$ is the deviatoric strain rate. In the energy equation, T is the temperature, C_P is the effective specific heat capacity, α is the effective thermal expansion coefficient, k is the thermal conductivity, and Q is the intrinsic specific heat production.

When using a thermodynamically consistent equation of state that contains phase transitions, solving this set of governing equations becomes challenging (Dannberg et al., 2022), especially when univariant phase transitions occur. First, the stable phase changes abruptly, with no mixed-phase region. Therefore, an infinitesimally small change in temperature or pressure may cause the material to change from 100% of a given phase to 100% of another phase. The resulting density oscillations can prevent convergence of the nonlinear solver for the coupled system (1)–(3). Second, the equations consider C_P and α to be the effective properties, which inherently account for latent heat release/absorption, as an alternative but equivalent approach to explicitly tracking phase functions (Christensen and Yuen, 1985). The effective properties are computed using the temperature derivatives of the total entropy and density, respectively, in a closed system at constant pressure at equilibrium phase assemblage. Both values have sharp spikes at phase transitions, and can even become infinite at univariant transitions. These discontinuities prevent the accurate representation of latent heat effects, causing spurious temperature oscillations in the numerical solution of the energy conservation equation (3) as material crosses these transitions (Dannberg et al., 2022).

2.1 Using entropy instead of temperature

To address the challenges discussed above, we employ and extend the entropy method discussed in our previous work (Dannberg et al., 2022). Instead of Equations (1)–(3), we instead consider the system of equations

$$-\nabla \cdot (2\eta\dot{\varepsilon}) + \nabla P = \rho_h \mathbf{g}, \tag{4}$$

$$\frac{\partial \rho_h}{\partial t} + \mathbf{u} \cdot \nabla \rho_h + \rho_h \nabla \cdot \mathbf{u} = 0, \text{ and} \tag{5}$$

$$\rho_h T \left(\frac{\partial S}{\partial t} + \mathbf{u} \cdot \nabla S \right) - \nabla \cdot (k \nabla T) = \rho_h Q + 2\eta\dot{\varepsilon} : \dot{\varepsilon}. \tag{6}$$

The approach applies the projected density approximation (Gassmöller et al., 2020), which accounts for the volume changes associated with compressibility, thermal expansion, and density variations caused by phase changes. These variations are modeled accurately not just on a reference profile (as for example defined by the anelastic liquid approximation, Jarvis and McKenzie, 1980), but for arbitrary temperature and pressure, for example, when changes in temperature shift a phase transition

https://doi.org/10.5194/egusphere-2026-1972
Preprint. Discussion started: 14 April 2026
© Author(s) 2026. CC BY 4.0 License.

to a different pressure. To avoid pressure oscillations, the projected density approximation uses the density ρ_h evaluated at the hydrostatic reference pressure ($P_h(z,T)$) instead of the density evaluated at the true simulation pressure (P).

Moreover, in Equation (6), we solve the energy equation for entropy instead of temperature. To do so, we obtain the equation of state—including the realistic phase transitions—from a material property table calculated by thermodynamics software (Connolly, 2009; Myhill et al., 2023, 2024) and based on a thermodynamic database (Stixrude and Lithgow-Bertelloni, 2022). In the table, pressure P and entropy S appear as independent variables, and we look up T and ρ. The entropy formulation does not contain α. C_P is only used in the thermal diffusion term (see Dannberg et al., 2022) where we solve the thermal diffusion problem separately and then use the solution to that problem in the entropy equation. Thus, the method can handle spikes in α and C_P without invoking numerical instability. In addition, entropy stays constant along an adiabat so that latent heat contributions do not have to be computed separately. Instead, the corresponding temperature change is naturally included in the lookup table. For more details on the original formulation, we refer the reader to Dannberg et al. (2022).

2.2 Introducing multiple chemical components

The entropy method as described by Dannberg et al. (2022) did not allow for chemical heterogeneity, which is common in the mantle. To extend the method to include multiple chemical components, we track the individual specific entropy S_i of each chemical component i as well as its mass fraction X_i:

$$\frac{\partial X_i}{\partial t} + \mathbf{u} \cdot \nabla X_i = 0 \tag{7}$$

$$\rho_{h,i} T \left(\frac{\partial S_i}{\partial t} + \mathbf{u} \cdot \nabla S_i \right) - \nabla \cdot (k \nabla T) = \rho_{h,i} Q + 2\eta \dot{\varepsilon} : \dot{\varepsilon} + q_{\mathrm{eq},i}, \tag{8}$$

where $\rho_{h,i}$ is the density of component i, computed using the hydrostatic pressure P_h and entropy S_i. Note that the evolution of each specific entropy implies a corresponding change in the component temperature $T_i(P_h, S_i)$. These T_i are generally not identical, as each component has its own adiabatic temperature gradient. But Equation 8 requires that there is only a single local temperature (T). We here make the thermodynamic assumption that each evaluation point thermally and mechanically equilibrates due to thermal diffusion and mechanical relaxation between components on a timescale significantly shorter than the numerical time step. This thermomechanical equilibration ensures that all components have the same temperature (and pressure) by modifying their individual entropies S_i such that the temperature of each component is the same ($T_i = T$). The additional constraint we apply on the equilibrium temperature is that the total entropy is unchanged by the thermal equilibration process, i.e., $\sum_i X_i \Delta S_{\mathrm{eq},i} = 0$, where X_i is the mass fraction of the component i, and $\Delta S_{\mathrm{eq},i}$ is its entropy change during the thermal equilibration. In Equation (8), this thermal equilibration step is associated with component-wise heating rates $q_{\mathrm{eq},i}$. We discuss the numerical implementation of this thermal equilibration process in Section 3.

The implicit assumptions of this scheme are (i) that individual chemical components do not chemically react with each other and (ii) that any stresses arising from differences in strain between components during changes in pressure and temperature can be relaxed without doing a significant amount of mechanical work. The latter assumption applies to any simulations modeling a single bulk composition with multiple physically-distinct phases, even if those phases are unreactive (i.e. the vast majority

https://doi.org/10.5194/egusphere-2026-1972
Preprint. Discussion started: 14 April 2026
© Author(s) 2026. CC BY 4.0 License.

of geodynamics simulations). Our implementation produces identical results in cases where two non-reactive subcomponents (e.g., olivine and orthopyroxene in the upper mantle) are either combined in a single lookup table, or separated into multiple lookups.

3 Numerical implementation

3.1 General Workflow

We have implemented the multicomponent entropy method in the community geodynamic modeling software ASPECT 3.1.0 (Heister et al., 2017; Kronbichler et al., 2012; Bangerth et al., 2024a, b; Clevenger and Heister, 2021; Gassmöller et al., 2020; Dannberg et al., 2022). The software and parameter files for all models presented in this work can be found in a Zenodo data repository accompanying this paper (Li et al., 2026).

We summarize the numerical algorithm in Figure 1. Each time step begins with a thermal equilibration step (described in Section 3.2) to ensure that all components have the same temperature T_{eq}. During this equilibration, we directly apply the entropy changes $\Delta S_{\mathrm{eq},i}$ to the individual entropies rather than including them as the additional term $q_{\mathrm{eq},i}$ when solving Equation (8).

Next, we start a non-linear iteration over the coupled system of advection and Stokes equations. We decouple the thermal conduction from the entropy equation (8) using an operator splitting scheme, first solving for thermal conduction of the equilibrated temperature. Then, we advect each chemical component (Equation 7) to obtain new mass fractions X_i. Using the previously computed conduction contribution, we then solve the advection equations (8) for the entropies S_i of each component. At this point, the chemical components are not thermally equilibrated, and therefore we perform the thermal equilibration again to obtain T_{eq} and $S_{\mathrm{eq},i}$. This allows us to use the equilibrated component entropies to look up the component densities $\rho_{h,i}$, compute ρ_h based on the component mass fractions X_i, and use the equilibrated temperature T_{eq} to compute the viscosity η. These material properties are required to solve the Stokes equations (4, 5). In case of convergence, this is the last step in the non-linear iteration loop; otherwise, we loop back to solving for thermal conduction with T_{eq}.

3.2 Thermal equilibration

As described in Section 2.2, we solve a separate advection equation (8) for each component, and the resulting entropies generally correspond to different component temperatures. To ensure that all components at a given location are at equal temperature, we perform a thermal equilibration step that adjusts the entropies of the individual components while conserving the total entropy. The method works as follows:

We start with the component entropies after advection ($S_i^{[0]}$), their mass fractions X_i, and the hydrostatic pressure P_h. First, we evaluate the unequilibrated temperature $T_i^{[0]} = T_i(P_h, S_i^{[0]})$ and specific heat $C_{Pi}^{[0]} = C_{Pi}(P_h, S_i^{[0]})$ of each component. To obtain the equilibrated values, we iterate over the following steps (with iteration number k):

https://doi.org/10.5194/egusphere-2026-1972
Preprint. Discussion started: 14 April 2026
© Author(s) 2026. CC BY 4.0 License.

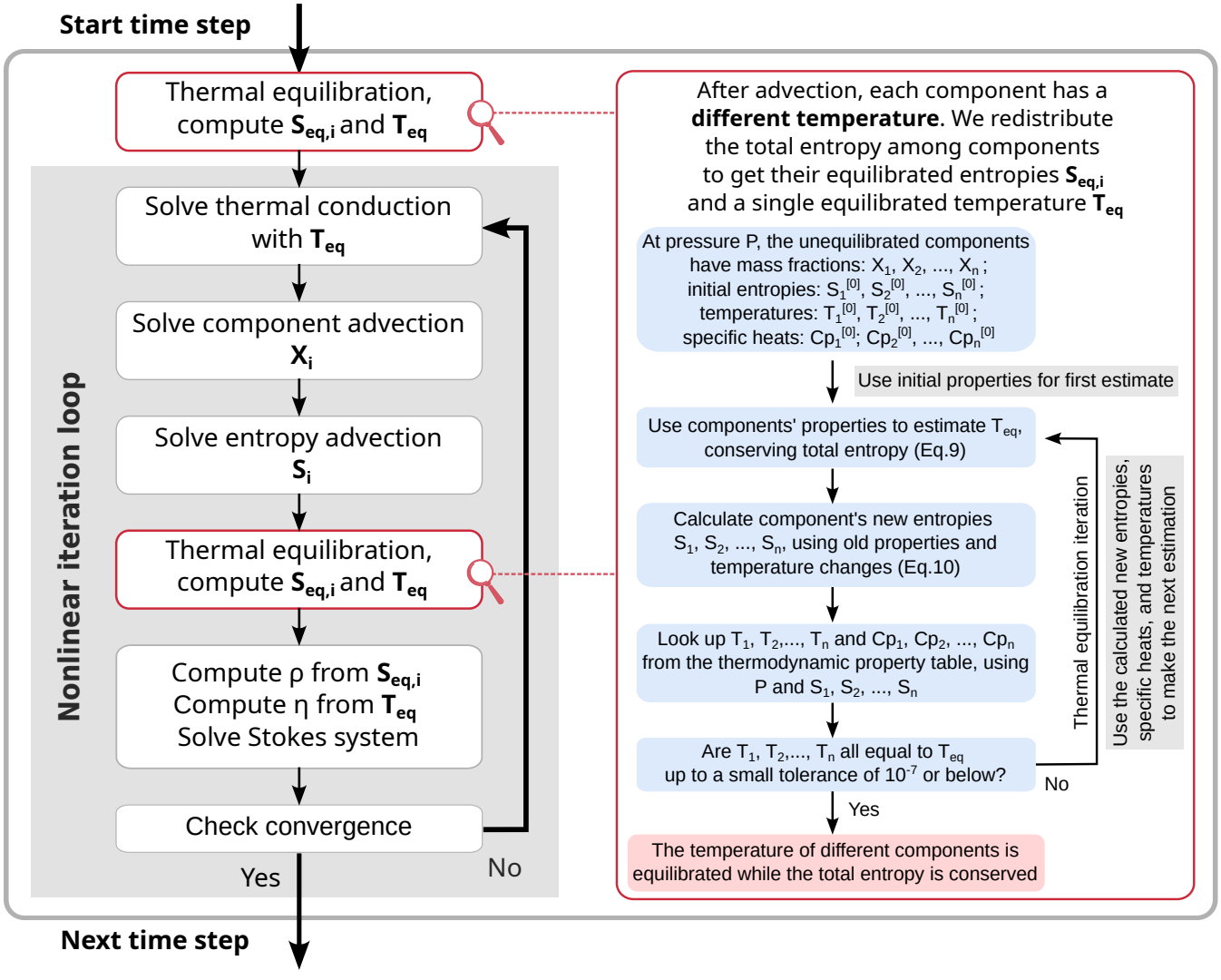

Figure 1. Flowchart of the solver procedure at each time step for the multi-component method.

https://doi.org/10.5194/egusphere-2026-1972
Preprint. Discussion started: 14 April 2026
© Author(s) 2026. CC BY 4.0 License.

1. Using the thermodynamic relation $dS = C_P/T\,dT = C_P\,d(\ln T)$, we can estimate a single temperature that conserves the total entropy, i.e. $\sum_i^n X_i \Delta S_{\mathrm{eq},i} = 0$, among all n components (see Appendix B for a derivation):

$$\ln T^{[k+1]} = \frac{\sum_{i=1}^{n} X_i C_{Pi}^{[k]} \ln T_i^{[k]}}{\sum_{i=1}^{n} X_i C_{Pi}^{[k]}} \tag{9}$$

   We here average $\ln(T)$ rather than T because at high temperature, C_P is almost constant in non-reacting media.

2. Calculate the new component entropies $S_i^{[k+1]}$ at the estimated $T^{[k+1]}$ by:

$$S_i^{[k+1]} = S_i^{[k]} + C_{Pi}^{[k]} \ln\left(\frac{T^{[k+1]}}{T_i^{[k]}}\right) \tag{10}$$

3. Evaluate the new temperature for each component $T_i^{[k+1]} = T_i(P_h, S_i^{[k+1]})$

4. Compare the individual $T_i^{[k+1]}$, exit the iteration if their absolute differences are equal within a given tolerance, repeat otherwise.

Then, we set the final $T_i^{[k]}$ as equilibrated temperature T_{eq}, and $S_i^{[k]}$ as new component entropies $S_{\mathrm{eq},i}$. We later use T_{eq} and $S_{\mathrm{eq},i}$ to solve equations (4)–(6).

The entropy change from unequilibrated to equilibrated ($\Delta S_{\mathrm{eq},i} = S_{\mathrm{eq},i} - S_i$) implies an inter-component heat transfer rate of $q_{\mathrm{eq},i} = \rho_{h,i} T \Delta S_{\mathrm{eq},i}/\Delta t$ (in W m^{-3}) in Equation (8), where Δt is the time step length. We treat this heat transfer as an instantaneous reaction, using an operator splitting scheme as described in the appendix of Dannberg et al. (2021) to directly apply the update $\Delta S_{\mathrm{eq},i}$ to the individual entropies rather than including $q_{\mathrm{eq},i}$ as an additional term when solving Equation (8).

3.3 Equation of state and preprocessing steps

Our implementation relies on the use of self-consistently calculated physical properties, which can be precomputed externally using thermodynamic modeling software such as HeFESTo (Stixrude and Lithgow-Bertelloni, 2005, 2011), PerpleX (Connolly, 2009), or BurnMan (Cottaar et al., 2014; Myhill et al., 2023), and stored as lookup tables. Since Eq. (8) operates in entropy–pressure space, these lookup tables need to be structured with entropy and pressure as independent variables, while temperature, density, and isobaric specific heat are properties defined as a function of those variables.

The isobaric specific heat is a second order derivative of the energy of a material, and as such its local values are dependent not only on state, but also on whether reactions between materials are allowed. In this study, look-up tables are formulated assuming that all reactions proceed rapidly, and so the effective isobaric specific heat is a function of those reactions. During perfectly univariant reactions, this heat capacity becomes infinite, which causes problems for the iterative scheme described by Equations (9) and (10). A related issue arises when two distinct compositions undergo the same univariant reaction (e.g., the coesite–stishovite transition); during the reaction, the partitioning of entropy between the compositions becomes undefined (Figure 2). This partitioning of entropy is just another way of describing the reaction progress in each material; it is equally

https://doi.org/10.5194/egusphere-2026-1972
Preprint. Discussion started: 14 April 2026
© Author(s) 2026. CC BY 4.0 License.

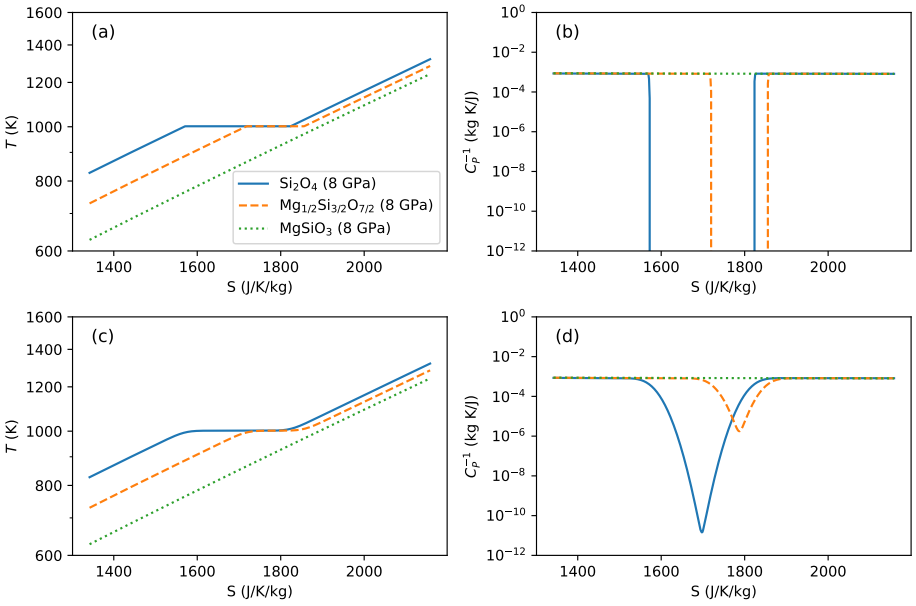

Figure 2. Thermal properties of rocks of three different compositions in the $MgSiO_3$-SiO_2 system at 8 GPa, as a function of specific entropy, according to the database of Stixrude and Lithgow-Bertelloni (2022). Temperature is plotted on a log scale. (a) As each of the three compositions are heated, their entropy increases. At low entropies, this entropy increase causes an increase in temperature. At higher entropies, the SiO_2-saturated assemblages pass through the stishovite-coesite boundary, which buffers the compositions at the transition temperature. Note that during this transition, two materials in contact could partition the entropy in many different ways. (b) The temperature buffering through univariant transitions results in the effective heat capacity becoming infinite (as the ratio of latent to sensible heat becomes infinite). (c) Gaussian smoothing of assemblage enthalpy resolves any ambiguity in partitioning of entropy between different compositions by removing any regions where $\partial T/\partial S = 0$. (d) The effective heat capacity after smoothing is no longer infinite within the univariant phase transition.

valid (mathematically) to assume that one material reacts first, or that all materials react at the same rate. This ambiguity must be resolved in any software implementation.

Several strategies can address these difficulties. Here, we adopt a simple and internally consistent approach by slightly smoothing the thermodynamic lookup tables to remove the singularities. Specifically, we first compute a P–S grid of specific
210 enthalpy ($\mathcal{H}$, J/kg), which is the thermodynamic potential with entropy and pressure as natural (independent) variables ($\mathcal{H} = \mathcal{H}(P, S)$). We then apply a two-dimensional Gaussian filter to this grid. From the smoothed enthalpy field, we recover the

https://doi.org/10.5194/egusphere-2026-1972
Preprint. Discussion started: 14 April 2026
© Author(s) 2026. CC BY 4.0 License.

required thermodynamic quantities using standard identities:

$$T = \left(\frac{\partial \mathcal{H}}{\partial S}\right)_P,$$

$$\rho = M\left(\frac{\partial \mathcal{H}}{\partial P}\right)_S^{-1},$$

$$C_P = T\left(\frac{\partial^2 \mathcal{H}}{\partial S^2}\right)_P^{-1}.$$

where M is the molar mass of the component, and S is the specific entropy.

4 Verification and Benchmarking

Having derived the method, numerical algorithm and preprocessing steps, we verify our implementation in a number of tests designed to benchmark individual aspects of the method and compare its results to known solutions. The material property tables and reference values in this section are generated using BurnMan and PerpleX using the mineral physics database from Stixrude and Lithgow-Bertelloni (2022) and Stixrude and Lithgow-Bertelloni (2011). More details on the lookup tables can be found in Appendix A.

Test 1: Thermal equilibration at constant pressure

We begin with a test that verifies the implementation of our temperature equilibration algorithm described in Section 3.2, specifically, convergence and accuracy of the iterative method. We constructed a simple system with two components: a single cell containing 70 wt% forsterite (Fo) (using Lookup table 1 described in Appendix A) and 30 wt% enstatite (En) (using Lookup table 2). We start with a significant contrast in the arbitrarily chosen initial component entropies: 2700 J/K/kg for Fo, 700 J/K/kg for En. All model boundaries are free-slip and insulating. There is no gravity and therefore a uniform pressure of zero applies throughout the domain.

No other computation than the thermal equilibration is performed in this test. We compare the equilibrated temperature with the exact value (1117.41136 K) for the same two-component mixture at a bulk entropy of 2100 J/K/kg and zero pressure. This bulk entropy is identical to our test model, since $S_{\text{bulk}} = \sum_i X_i S_i$, with X_i the mass fraction and S_i the specific entropy of component i.

Our model equilibrates within only a few iterations, with an equilibration tolerance of 10^{-7} K. The relative error scales with the resolution of the lookup table (see Table 1), and results from small inaccuracies arising from the interpolation of the lookup table. Our equations and implementation successfully equilibrate materials even for large differences in initial entropy and temperature, much larger than expected for typical time steps in application cases.

Test 2: Thermal equilibration with changing pressure

Our second test is identical to Test 1, except that pressure increases over time. Since our method conserves the total entropy during the equilibration, this setup is representative of moving material from the surface to increasing depth along an adiabat.

https://doi.org/10.5194/egusphere-2026-1972
Preprint. Discussion started: 14 April 2026
© Author(s) 2026. CC BY 4.0 License.

Table 1. Convergence results of Test 1 with an equilibration tolerance of 10^{-7} K. The ASPECT results converge towards the exact prediction with decreasing entropy grid spacing of the lookup table, showing the resolution of the used table controls the accuracy of the equilibration routine.

Entropy grid spacing (J/K/kg)	Iteration count	T_{eq} (K)	Relative error
24	6	1117.43082	1.74×10^{-5}
12	5	1117.41701	5.06×10^{-6}
6	4	1117.41359	2.00×10^{-6}
Exact value		1117.41136	

Table 2. Results of Tests 2, 3, and 8. We compare the temperature and density at the maximum model pressure with exact expected values (Tests 2 and 3) or a reference model with an equilibrium composition (Test 8). The relative errors are shown in the gray rows.

	Test 2	Test 3	Test 8 (2 comps)	Test 8 (3 comps)
Component 1	Fo	Fo	Qtz⇔Coe (60 wt%) + En (40 wt%)	Qtz⇔Coe (60 wt%) + En (40 wt%)
Comp. 1 wt%	70	70	70	35
Component 2	En	En	Qtz⇔Coe (40 wt%) + En (60 wt%)	Qtz⇔Coe (60 wt%) + En (40 wt%)
Comp. 2 wt%	30	30	30	35
Component 3	/	/	/	Qtz⇔Coe (60 wt%) + En (40 wt%)
Comp. 3 wt%	/	/	/	30
Bulk entropy (J/K/kg)	2100	2100	1728.8	1728.8
P (GPa)	40	40.66	2.8	2.8
T (K)	1320.72368	1322.53	1029.10691	1029.10691
T_{ref}	1320.69756	1322.52230	1029.10631	1029.10631
T Error	1.98×10^{-5}	5.82×10^{-6}	5.83×10^{-7}	5.83×10^{-7}
ρ (kg/m^3)	3897.46158	3906.43	3149.26299	3149.26299
ρ_{ref} (kg/m^3)	3897.46270	3906.45840	3151.17691	3151.17691
ρ Error	2.87×10^{-7}	7.27×10^{-6}	6.07×10^{-4}	6.07×10^{-4}

The temperature of the two-component material in our test closely follows the exact isentrope with a relative error of $\sim 2 \times 10^{-5}$ (Figure 3, compare dashed orange line with the solid blue line). Table 2 lists the exact temperature and density values, along with the relative errors at $P = 40$ GPa. In this test, we suppress all equilibrium phase transformations (see Appendix A).

https://doi.org/10.5194/egusphere-2026-1972
Preprint. Discussion started: 14 April 2026
© Author(s) 2026. CC BY 4.0 License.

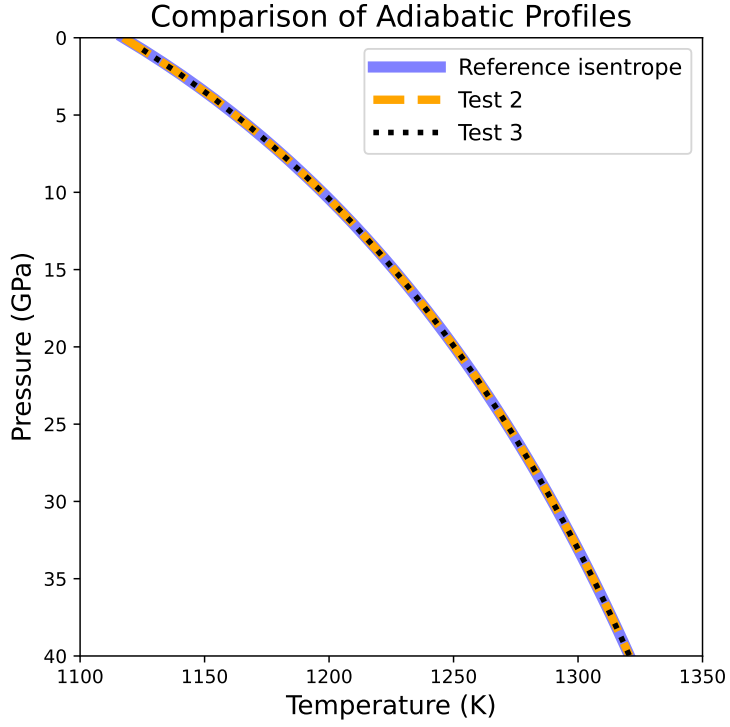

Figure 3. Results of Tests 2 and 3. The blue solid line shows the expected isentropic profile; the dashed orange lines shows ASPECT's results for Test 2, where the temperature changes due to a given pressure change over time; and the black dotted line shows ASPECT's results for Test 3, where the temperature changes spatially along an isentrope as material flows through a pipe where pressure increases with depth.

Test 3: Thermal equilibration of material in motion

To test whether the thermal equilibration works correctly in a moving medium, we implement a repeat of Test 2 in a 1D simulation. Material flows through a vertical pipe that is 1400 km long under a gravity of g = 9.81 m/s^2 and without thermal conduction ($k = 0$ W/m/K). As in Tests 1 and 2, the initial composition is a mixture of 70 wt% Fo with an entropy of 2700 J/K/kg, and 30 wt% En with an entropy of 700 J/K/kg using the same lookup tables as in Tests 1 and 2. At both side boundaries of the pipe, a vertical downward velocity of 0.01 m/year is prescribed, and the inflowing material has the same composition and entropy as in the initial conditions. The bottom boundary is open to allow for outflow. Since there is no conduction or mechanisms of internal heating (e.g., shear or radioactivity), material should flow downward along an isentrope until it exits the model with a higher temperature. The expected solution of this benchmark is identical to Test 2, and the close agreement can be seen in Figure 3. The second column of Table 2 shows that the test exhibits a relative error less than 10^{-5} at 40.66 GPa (the bottom of the pipe).

https://doi.org/10.5194/egusphere-2026-1972
Preprint. Discussion started: 14 April 2026
© Author(s) 2026. CC BY 4.0 License.

Table 3. Results of Test 4. The reference temperature is obtained from a model using the classical pressure–temperature formulation. Temperatures are compared at 6 GPa and 200 Myr. The relative error decreases with decreasing time step size.

Time step size (years)	Temperature (K)	Reference temperature (K)	Relative error
3×10^7	1147.51	1146.31	1.05×10^{-3}
3×10^6	1147.08	1146.85	2.01×10^{-4}
3×10^5	1147.05	1146.91	1.22×10^{-4}
3×10^4	1147.05	1146.92	1.13×10^{-4}

Test 4a: Heat conduction along an adiabat

In Test 3, we showed that thermodynamic quantities evolve appropriately during advection. In Test 4, we ensure that conduction along an adiabat is also treated correctly. We start from the final (steady-state) result of Test 3—a 1D isentropic profile—and stop all movement by closing the top and bottom boundaries and applying free slip conditions to all boundaries. We now introduce conduction by setting the thermal conductivity to 4.7 W/m/K. The temperature of the top boundary is fixed to 1117.41136 K, as in Test 1. All other boundaries are thermally insulating. Compared to the setup of Test 3, we reduce the length of the pipe to 200 km for computational efficiency. The model is run for 3 billion years, after which thermal conduction has resulted in a uniform temperature throughout the model domain (Figure 4, panel A). This setup follows Benchmark A3 from Dannberg et al. (2022).

As no analytical solution is available for the thermal evolution of this test, we compare our results to a more conventional model with the same setup, but using a pressure–temperature lookup table. Because no phase transitions occur within the domain, the classical energy equation formulated in P–T space (Eq. 3) is sufficient to accurately solve this conduction problem. We evaluate the temperature profiles of both models at different points in time, and find that they show consistent behavior (Figure 4A, compare the red and gray lines). To quantify convergence of the solution, we compare the temperature at 6 GPa after 200 Myr of model evolution time. As expected, the relative temperature difference between the two models decreases with decreasing time step size (Table 3), reaching 1.13×10^{-4} at a time step size of 3×10^4 years.

Test 4b: Heat conduction with spatially variable composition

The previous tests demonstrate that the method correctly captures heat transport with multiple chemical components distributed uniformly throughout the model. We now extend Test 4a to include spatial variations in composition to show that the components thermally equilibrate and heat is conducted along an adiabat in a chemically heterogeneous domain. From top to bottom, the mass fraction of Fo increases linearly from 0% to 100%, and En correspondingly decreases from 100% to 0%. Both components have thermal conductivities of 4.7 W/m/K. At every depth of this pipe, the composition is different, but the initial bulk entropy remains constant at 2100 J/K/kg.

https://doi.org/10.5194/egusphere-2026-1972
Preprint. Discussion started: 14 April 2026
© Author(s) 2026. CC BY 4.0 License.

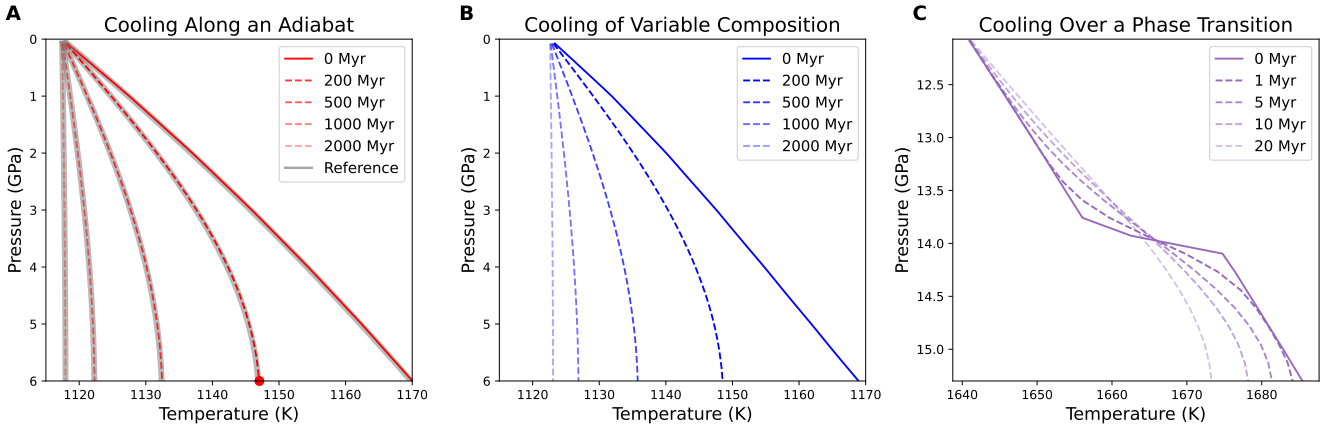

Figure 4. Vertical temperature evolution of Tests 4a (panel A, results shown for $\Delta t = 3 \times 10^5$ years), 4b (panel B, $\Delta t = 3 \times 10^5$ years), and 4c (panel C, $\Delta t = 1 \times 10^4$ years). In all panels, the initial temperature profiles are shown as solid lines. Vertical temperature profiles at later times are plotted as dashed lines, with fainter colors representing later times. In panel A, the reference temperature from the classical P–T formulation is shown as a solid gray line, plotted below the model solution indicated by red lines. The red dot marks the temperature and pressure used to compute the errors in Table 3

In the first time step, the two components thermally equilibrate while the bulk entropy is spatially uniform. The top boundary has an equilibrated temperature of 1123.34 K. As time proceeds, the temperature in the pipe gradually decreases and eventually equilibrates to the temperature value at the top boundary (Figure 4B). While there is no analytical or reference solution for this test case, it captures the correct equilibrium state, and it shows a similar evolution as case 4a. Differences between 4a and 4b are caused by the different starting adiabats, but also slightly different densities and specific heat between the cases, which affects the time scale of thermal conduction.

Test 4c: Heat conduction along an adiabat crossing a phase transition

This test determines whether heat is conducted correctly across a phase transition along an adiabat. The setup follows Test 4a, but uses a different bulk composition, pressure range, and end time. The model has a uniform Mg_2SiO_4 composition throughout the domain, with 30% of a component consisting of the equilibrium phase of either forsterite or Mg-wadsleyite (Wad) (Lookup table 3 described in Appendix A), and 70% of a component that is always pure forsterite (Lookup table 1). The transition in the first component is univariant, representing the sharpest possible transition and therefore the most challenging transition to simulate. Both components start with an initial entropy of 2480 J/K/kg.

The model geometry is a pipe extending 100 km in length. The pressure at the top boundary is set to 12.0 GPa and increases with depth, controlled by the density and the gravity $g = 9.8$ m s^{-2}. The phase transition occurs at approximately 13.85-14 GPa, corresponding to a depth of approximately 55–60 km from the top of the domain.

https://doi.org/10.5194/egusphere-2026-1972
Preprint. Discussion started: 14 April 2026
© Author(s) 2026. CC BY 4.0 License.

Table 4. Results of Test 5. This test includes four different initial entropy combinations. The smaller the density change during equilibration, the smaller the mass conservation error between the initial time step (time step 0) and time step 3. After time step 3, mass is conserved, as shown in Table 5.

Initial entropy of Forsterite (70 wt%)	Initial entropy of Enstatite (30 wt%)	Relative density change during equilibration	Relative mass error (equilibration in time step 1)	Relative mass error (equilibration in time step 2)
2700	700	$1.11393376 \times 10^{-2}$	5.50777×10^{-3}	9.20195×10^{-5}
2200	1000	3.1906558×10^{-3}	1.58992×10^{-3}	7.60854×10^{-6}
2100	2100	7.23747×10^{-6}	3.06294×10^{-6}	0
2102.496	2094.175	0	0	0

Table 5. Results of Tests 5 (left columns) and 6 (right columns). Comparing aross different model resolutions, mass conservation in Test 5 always stands. The data for Test 5 listed in the table are taken from its second case, which has initial entropies of 2200 and 1000 J/K/kg for Fo and En, respectively. In Test 6, the topographic error decreases with increasing number of mesh cell. The reference topographic change is calculated analytically using density changes computed by BurnMan.

	Mass Conservation Test (5)		Volume Change Test (6)	
#cells in model domain	Relative mass conservation error (time step 0–3)	Relative mass conservation error (time step 3–30)	Rate of topographic change (m/year)	Relative topographic error
1	1.58992×10^{-3}	0	$9.96820156 \times 10^{-3}$	6.66018×10^{-7}
4^1	1.58992×10^{-3}	0	$9.96819771 \times 10^{-3}$	2.79790×10^{-7}
4^2	1.58992×10^{-3}	0	$9.96819719 \times 10^{-3}$	2.27624×10^{-7}
4^3	1.58992×10^{-3}	0	$9.96819709 \times 10^{-3}$	2.17592×10^{-7}
Reference			$9.96819492 \times 10^{-3}$	

The results of this test demonstrate two expected behaviors (Figure 4C): (1) the temperature discontinuity at the phase transition caused by latent heat release diffuses over time, and (2) the overall temperature profile gradually cools because the top boundary is held at a fixed pressure of 12 GPa and entropy of 2480 J/K/kg.

Test 5: Mass conservation during thermal equilibration

We have established so far that the temperature and entropy are computed correctly during advection and conduction, but we also need to ensure that mass is conserved during the equilibration, i.e., that the volume change of material is consistent with the density change. This effect cannot be captured by geodynamic models using the Boussinesq/anelastic liquid approximation, but should be correctly captured by the projected density approximation (Gassmöller et al., 2020).

https://doi.org/10.5194/egusphere-2026-1972
Preprint. Discussion started: 14 April 2026
© Author(s) 2026. CC BY 4.0 License.

This test consists of a single cell (13,000 m × 13,000 m), with a free top boundary that allows the material to expand freely and deform the domain, while all other boundaries are closed. Both gravity and thermal conductivity are set to 0. The initial composition follows Test 1, with 70 wt% Fo and 30 wt% En. The system is thermally insulated, and the only process occurring is thermal equilibration among the components, which takes place during the first time step after initialization, hereafter referred to as Time Step 1. During thermal equilibration, the densities of the individual components change, leading to a change in bulk density and therefore a change in volume. After this local equilibration, we expect no further expansion, contraction, or motion in the model. Since no material is added to or removed from the model domain, the total mass should be conserved.

We compare four different initial entropy conditions for the components with varying degrees of deviation from the equilibrium temperature, listed in Table 4, which result in distinct density changes after equilibration. The largest relative density increase among the four cases occurs for initial entropies of Fo and En of 2700 J/K/kg and 700 J/K/kg, respectively, which increases the averaged density by 1.1%, from approximately 3105 kg/m^3 to 3139 kg/m^3. The other extreme case occurs for an initial Fo and En entropy of 2102.496 J/K/kg and 2094.175 J/K/kg, respectively, which corresponds to thermal equilibrium and therefore no density change is expected. We measure the error of the equilibration algorithm by tracking the total mass in the model domain over time, for which we compute $m(t) = \int_{\Omega} \rho_{\text{bulk}}(\boldsymbol{x}, t) d\boldsymbol{x}$, where $\boldsymbol{x}$ denotes the spatial coordinate, t is time, ρ_{bulk} is the bulk density, and Ω the (time-dependent) domain volume.

The results show that our implementation does conserve mass (rightmost column in Table 4 and left column in Table 5), however, there are two sources of error, a transient error which results from the algorithmic implementation, and a persistent error which is inherent to the test design. First, in the equilibration time step we observe a spike in the mass conservation error that disappears in the next time step, which is when the topography is adjusted according to the computed velocity. We confirmed in an experiment that this error spike disappears if the topography is adjusted immediately after solving the Stokes equation, but this modification is not currently supported in ASPECT. A permanent solution would require reordering of ASPECT's time-stepping scheme, which seems unnecessary as the apparent error only results from a delayed application of the correct mesh deformation. Second, thermal equilibration in our algorithm occurs in Time Step 1, during the initialization phase of the BDF2 time stepping scheme, which is performed using a first-order time step and therefore reduced accuracy. If equilibration is delayed to Time Step 2, when BDF2 is already properly initialized, the error is reduced by 2 orders of magnitude (compare two rightmost columns of Table 4). After the initial equilibration, mass is conserved throughout the model as expected (second column in Table 5).

Comparing the four initial entropy conditions (Table 4), we find that the mass conservation error depends on the relative density change during thermal equilibration: the smaller the density change, the smaller the mass conservation error. In the worst case scenario, where density increases by 1.11% in Time Step 1, an artificial mass increase of 0.55% (or 50% of the expected volume change) occurs during the first time steps. In contrast, when the model starts from thermally equilibrated entropies and no density change occurs, the artificial mass increase is zero. In addition, we repeat the second case (Fo entropy 2200 J/K/kg, En entropy 1000 J/K/kg) at different spatial resolutions and show that the mass error is independent of model resolution (Table 5), which supports our analysis that the error is caused by the initialization of the time-stepping scheme.

https://doi.org/10.5194/egusphere-2026-1972
Preprint. Discussion started: 14 April 2026
© Author(s) 2026. CC BY 4.0 License.

This error has no significant effect on model accuracy because it occurs only at the very beginning and does not accumulate over time. Moreover, the worst-case scenario we show represents an extreme edge case. In realistic setups, extreme initial temperature contrasts such as in the first case are unlikely. Instead, conditions are more comparable to the third case, in which the two components have similar but not fully equilibrated temperatures. As a result, the density does not change significantly during equilibration, and the artificial mass conservation error is small. If initializing the model components with (almost) equilibrated temperatures is impossible, we recommend delaying the equilibration to time step 2 to avoid the initial error in mass conservation.

Test 6: Volume change during continuous non-equilibrated inflow

Building on Test 5, which concerns mass conservation during one initial thermal equilibration step, we also test that the volume changes correctly with the density during thermal equilibration occuring during model evolution. Again, the model setup is a box with an initial size of 13,000 m $\times$ 13,000 m. The model has the same initial composition and component entropies as the second case from Test 5, consisting of 70 wt% Fo with an entropy of 2200 J/K/kg and 30 wt% En with an entropy of 1000 J/K/kg (Table 4, second row). The thermal conductivity and gravity are zero. Unequilibrated material flows into the box through a prescribed upward velocity of 0.01 m/year at the bottom boundary. The left and right boundaries are free-slip, permitting tangential flow, and the top boundary is a free surface that allows the volume to change freely. During the simulation, the domain therefore grows vertically, and the resulting topography changes account for both the material inflow and the volume change caused by equilibration. As in Test 5, Case 2, thermal equilibration causes a density increase from 3152.795 to 3162.854 kg/m^3, or 0.319%. Since mass should be conserved, we expect a corresponding volume contraction of $\Delta V = 1 - (3152.795/3162.854) = 0.318\%$. Therefore, as the new unequilibrated material flows in with a velocity of $u_y =$ 0.01 m/yr and equilibrates, we expect a surface topographic change of $u_y(1 - \Delta V) \approx 9.968 \times 10^{-3}$ m/yr.

Our results (Table 5) show that the rate of topographic increase (averaged over the last 10 time steps) only deviates by $\approx 6.66 \times 10^{-7}$ at the coarsest resolution (1 mesh cell). The relative error decreases linearly with increasing resolution, and stagnates around 2×10^{-7}. This very small remaining error is likely caused by the first-order accuracy of the free-surface advection algorithm.

Test 7a: Enthalpy change

In this test, we determine whether heating of the model domain correctly increases the internal energy. The setup is identical to the first case of Test 5 (first row of Table 4), except that now there is a constant heat inflow, either from a prescribed heat flux at the bottom boundary or from volumetric radiogenic heating. We test these two different heat sources because they are incorporated in different parts of the numerical algorithm: the boundary heat flux is included in the conduction term and solved via operator splitting (Dannberg et al., 2022, Equation 12, see also Section 3.1), while radiogenic heating is accounted for when we solve the advection equations for the component entropies (Equation 8). The thermal conductivity is set to a high value ($k = 1000$ W m^{-1} K^{-1}) to ensure near-instantaneous temperature equilibration across the domain. Our method remains

https://doi.org/10.5194/egusphere-2026-1972
Preprint. Discussion started: 14 April 2026
© Author(s) 2026. CC BY 4.0 License.

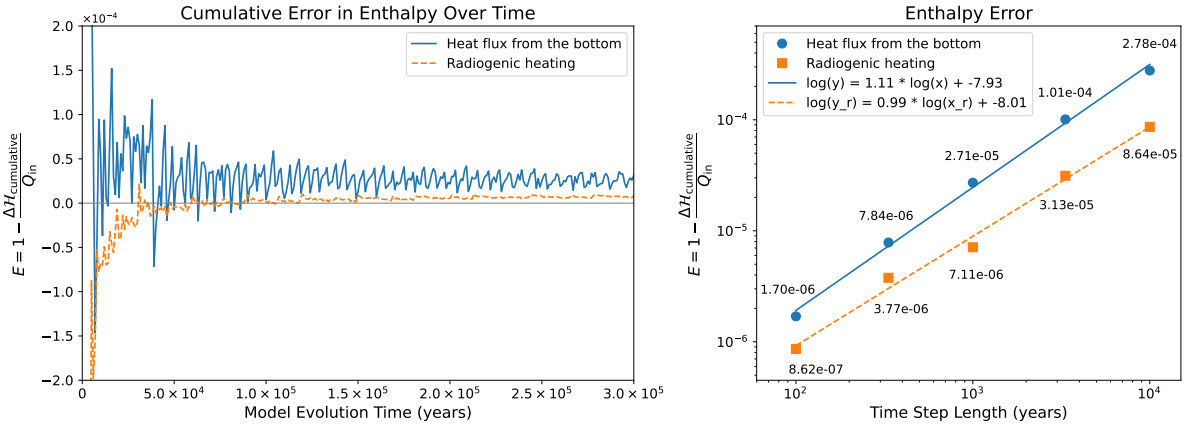

Figure 5. Results of Test 7a. Left panel: Evolution of the cumulative error over time. The blue line represents the model heated from the bottom and the orange line represents the model heated by radiogenic heating. Both models have a time step size of 1000 years. Right panel: Convergence of the error with respect to time step size for models with time step sizes from 100 to 10,000 years. E is computed as the average cumulative error over the last four time steps shown in the left panel, in order to mitigate the influence of small oscillations

stable for large thermal conductivity and time steps because the conduction term is solved implicitly. In this setup, we aim to equilibrate the temperature rather than to accurately solve the conduction, which is further simplified by the single-cell setup.

For models with heat flowing in from the bottom boundary, the cumulative heat addition is computed as:

$$Q_{\text{in}}^{\text{boundary}} = qLt$$

where q is the prescribed boundary heat flux density (0.05 W/m), L is the boundary length (13,000 m), and t is duration of heating that is considered for the test. The cumulative radiogenic heat addition is computed as:

$$Q_{\text{in}}^{\text{radiogenic}} = H_{\text{radiogenic}} M t$$

where $H_{\text{radiogenic}}$ is the specific radiogenic heating rate (10^{-8} W/kg) and M is the total mass of the material in the model. Since q and $H_{\text{radiogenic}}$ are prescribed, $Q_{\text{in}}^{\text{boundary}}$ and $Q_{\text{in}}^{\text{radiogenic}}$ can be calculated and serve as analytical reference solutions.

At constant pressure and with the absence of any other types of energy, the first law of thermodynamics gives $Q = \Delta\mathcal{H}$, where $\mathcal{H}$ is enthalpy. In differential form and in the absence of deviatoric stresses, $d\mathcal{H} = d\mathcal{U} + d(PV) = TdS - PdV + PdV + VdP = TdS + VdP$, where $\mathcal{U}$ is the internal energy. Therefore, as long as the pressure stays constant during the model evolution, the heat added to the model should be equal to the increase in enthalpy, which can be written as an integral over an entropy-volume path $\Gamma(S,V)$:

$$\Delta\mathcal{H}_{\text{cumulative}} = \int_{\Gamma(S,P=\text{constant})} T(S, P = \text{constant})\, dS.$$

https://doi.org/10.5194/egusphere-2026-1972
Preprint. Discussion started: 14 April 2026
© Author(s) 2026. CC BY 4.0 License.

Discretizing this integral, we obtain

$$\Delta\mathcal{H}_{\text{cumulative}} = \sum_{k=j}^{n} \frac{1}{2}(\bar{T}_k + \bar{T}_{k+1})(S_{k+1} - S_k).$$

For this particular test, the pressure is equal to zero throughout the domain, so the sources of heat all contribute to the local internal energy, and $\Delta\mathcal{H}$ is identical to $\Delta\mathcal{U}$.

We compare the numerical solution, $\Delta\mathcal{H}_{\text{cumulative}}$ with the analytical solution, Q_{in}, and quantify the error as $E = 1 - \Delta\mathcal{H}_{\text{cumulative}}/Q_{\text{in}}$, i.e. the cumulative error in enthalpy change over time relative to the added heat. After an initial spike up to a value of 2×10^{-4} the error decreases over time and stabilizes below 5×10^{-5} (Figure 5a). A log–log plot of error E against time step size at $t = 3 \times 10^5$ yrs indicates nearly linear convergence rates, with slopes of 1.11 for models with boundary heat flux and 0.99 for models with radiogenic heating (Figure 5). This is the expected convergence rate for a first-order operator splitting method (Dannberg et al., 2022; Gassmöller et al., 2020). This model setup therefore conserves energy with a small and time-step-dependent error.

Test 7b: Enthalpy change across a phase transition

Test 7a verifies that energy is correctly converted and that the total energy is conserved for an unchanging phase assemblage. To assess whether the enthalpy increases correctly during heating in the presence of a phase transition, we rerun the bottom heating case of Test 7a using two different components, both with an Mg_2SiO_4 composition: Component one with 50 wt% is always comprised of forsterite (Lookup table 6 in Appendix A) and component two with the other 50 wt% is comprised of forsterite or wadsleyite depending on entropy and pressure.

We test two cases. In the first case, we artificially reposition the forsterite to wadsleyite transition to intersect a 0 GPa isobar at 1200 K (Lookup table 4 in Appendix A). The shifted phase transition occurs between an entropy of 2170 and 2195 J/K/kg. The model starts with both components at an initial entropy of 2100 J/K/kg, and heats up for 5×10^6 years with a heat inflow of 0.05 W/m, allowing the second component to transition to the higher temperature phase (forsterite) during the heating process. The time step size is 10^4 years.

In the second case, we use an unmodified forsterite to wadsleyite phase transition (Lookup table 5). Correspondingly, we apply a constant pressure of 13 GPa to the upper boundary of the model while gravity is still kept at zero, such that the whole domain remains at the same constant pressure. We use the same heating rate and time step size as in the first case but use different entropies for the two components, namely 1950 J/K/kg for component one and 2300 J/K/kg for component two. As heat flows in, the temperature rises and the material crosses the phase transition over the interval of 2–3 Myr, in the entropy range of 2180–2204 J/K/kg, corresponding to a temperature of 1322.5 K.

We analyze the results using the same cumulative error E as in Test 7a, however, we here use a numerically simpler (but mathematically equivalent) approach to compute the error by looking up the current model $\mathcal{H}_{\text{cumulative}}(S, P)$ in the lookup table of each component, computing $\Delta\mathcal{H}$ as the difference between the current value and the equilibrated starting value, and summing $\Delta\mathcal{H}$ of both components weighted by mass fraction. This value is then used to compute $E = 1 - \Delta\mathcal{H}_{\text{cumulative}}/Q_{\text{in}}$ at any point in time and plotted in the top row in Figure 6. The first case (0 GPa) is plotted as a green line in the left column,

https://doi.org/10.5194/egusphere-2026-1972
Preprint. Discussion started: 14 April 2026
© Author(s) 2026. CC BY 4.0 License.

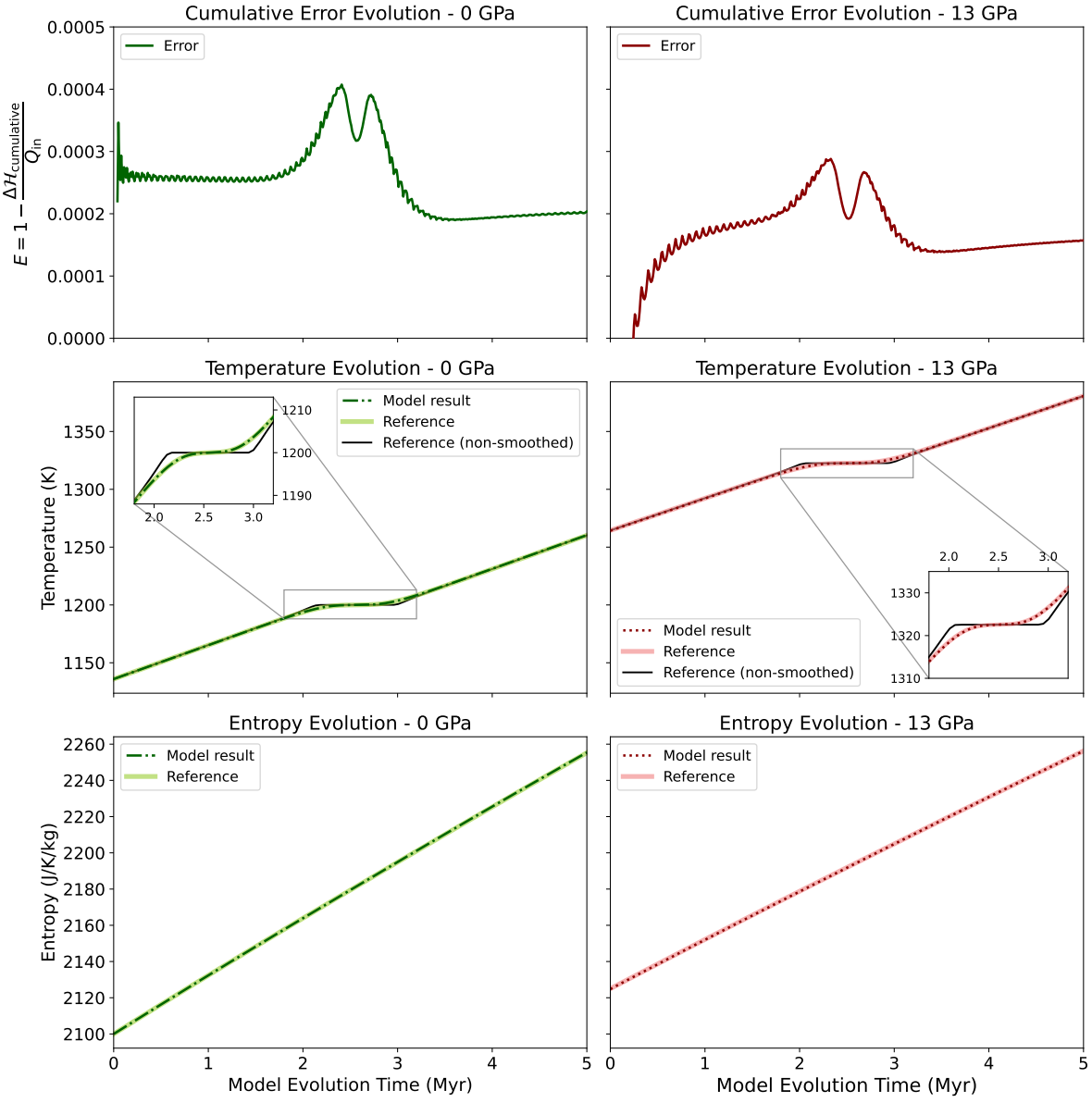

Figure 6. Cumulative error, temperature, and entropy evolution for the two test cases in Test 7b. Both models use a time step size of 10^4 years. The left column shows Case 1, where the Fo–Wad transition is artificially placed at 0 GPa, and the right column shows Case 2, with the transition at its original pressure (13 GPa). First row: Evolution of the cumulative error E over time. E is highest within the phase transition interval. Middle row: The model temperature remains nearly constant during the phase transition and is consistent with the reference value computed independently from the same lookup table. A reference temperature curve from a non-smoothed table shows the influence of smoothing on the temperature inside the phase transition. Bottom row: The entropy remains consistent with the reference solution as expected.

https://doi.org/10.5194/egusphere-2026-1972
Preprint. Discussion started: 14 April 2026
© Author(s) 2026. CC BY 4.0 License.

and the second case (13 GPa) is plotted as a red line in the right column. In both cases, the error E initially oscillates around a constant value of approximately 2×10^{-4}. A similar constant error was observed in Test 7a, where we show that it scales with the time step size and is therefore likely related to our time stepping scheme. The small oscillations appear at a frequency that corresponds to the grid spacing of the lookup tables used in the test. When changing the lookup table resolution, the frequency changes, indicating that the oscillations are related to interpolation errors when constructing or reading from the tables. When the model enters the P–T range of the phase transition, the error increases in two spikes situated at the beginning and end of the phase transition, reaching $\approx 4 \times 10^{-4}$ in Case 1. After the phase change is complete, E decreases again to $\approx 2 \times 10^{-4}$. The second case at realistic pressures for this phase transition (right column) behaves similarly. The error reaches a maximum value of $\approx 3 \times 10^{-4}$ at the beginning and end of the phase transition, then decreases to $< 2 \times 10^{-4}$ when the phase change is complete. Despite the temporarily increased E, the subsequent decrease at the completion of the phase change indicates that most of the artificially accumulated enthalpy during the phase transition is lost again, and overall enthalpy changes across the transition are small. Even at the center of the phase transition, where E is highest, the model's average temperature differs from the reference value computed from the same table by only < 0.03 K (Figure 6, middle row), and the entropy does not deviate noticeably from the reference value (bottom row), suggesting that the method is sufficiently accurate to resolve even sharp phase transition.

Test 8: Multiple components undergoing the same univariant transition

In the tests above, we demonstrate that advection, diffusion, mass and energy conservation are all handled correctly by our multi-component averaging algorithm, both in the absence of phase transitions and with a single component undergoing a univariant phase change. However, we must also consider the special case in which two or more components undergo the same univariant transition. As discussed in Section 3.3, a perfectly univariant phase transition has an infinite effective C_P, and will result in a non-unique solution for the partitioning of entropy between different components (Figure 2). In contrast, slightly smoothed lookup tables with sharp but finite spikes in C_P lead to well-defined partitioning of entropy between components.

This test setup is similar to that of Test 2. For simplicity, we use components composed of mixtures of quartz (qtz), which undergoes the quartz–coesite univariant transition, and enstatite, as these two minerals do not react with each other. Specifically, we compare three models containing different components in varying proportions but sharing the same bulk composition and total entropy, which should therefore lead to the same temperature evolution over time:

1. A single-component model with 54 wt% Qtz and 46 wt% En (Lookup table 9 in Appendix A) and an initial entropy of 1728.8 J/K/kg. Since there is only one component undergoing the phase transition, there is a unique solution even without smoothing, and we will therefore use this model as a reference solution.

2. A two-component model with 70 wt% component 1 + 30 wt% component 2. Component 1 consists of 60 wt% Qtz + 40 wt% En (Lookup table 8) and has an initial entropy of 1610 J/K/kg. Component 2 consists of 40 wt% Qtz + 60 wt% En (Lookup table 7), with an initial entropy of 2006 J/K/kg.

https://doi.org/10.5194/egusphere-2026-1972
Preprint. Discussion started: 14 April 2026
© Author(s) 2026. CC BY 4.0 License.

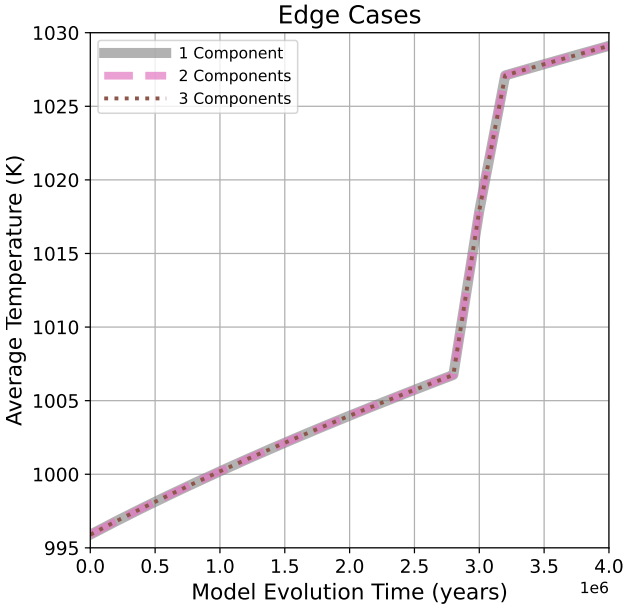

Figure 7. Results of Test 8. The thick gray line in the lower layer shows the reference solution obtained from a model using a single-component equilibrium table. The pink dashed line shows the results for the two-component model, and the dotted purple line shows the three-component model results. All lines lie on top of each other. The univariant phase transition occurs after pressure is increased for approximately 3 Myr, causing a sharp temperature increase, reflected in the increased slope of the curves.

3. A three-component model with 35 wt% component 1 + 35 wt% component 2 + 30 wt% component 3. Component 1 and 2 both contain 60 wt% Qtz + 40 wt% En (Lookup table 8), but start with different initial entropies (1600 J/K/kg and 1620 J/K/kg, respectively). Component 3 contains 40% Qtz + 60% En (Lookup table 7), with an initial entropy of 2006 J/K/kg.

For all three models, the pressure of the domain increases from 1.2 GPa to 2.8 GPa over 4 Myr. At approximately 2.4 GPa, the univariant reaction from quartz to coesite occurs. The computed temperatures in the two- and three-component models are identical within the available accuracy of the output. Moreover, they agree with the single-component model within a relative error of 5.83×10^{-7} (see Figure 7 and the third and fourth columns in Table 2). This result demonstrates that our method robustly handles this otherwise challenging scenario with negligible error as long as the lookup tables contain a large but finite spike in C_P.

https://doi.org/10.5194/egusphere-2026-1972
Preprint. Discussion started: 14 April 2026
© Author(s) 2026. CC BY 4.0 License.

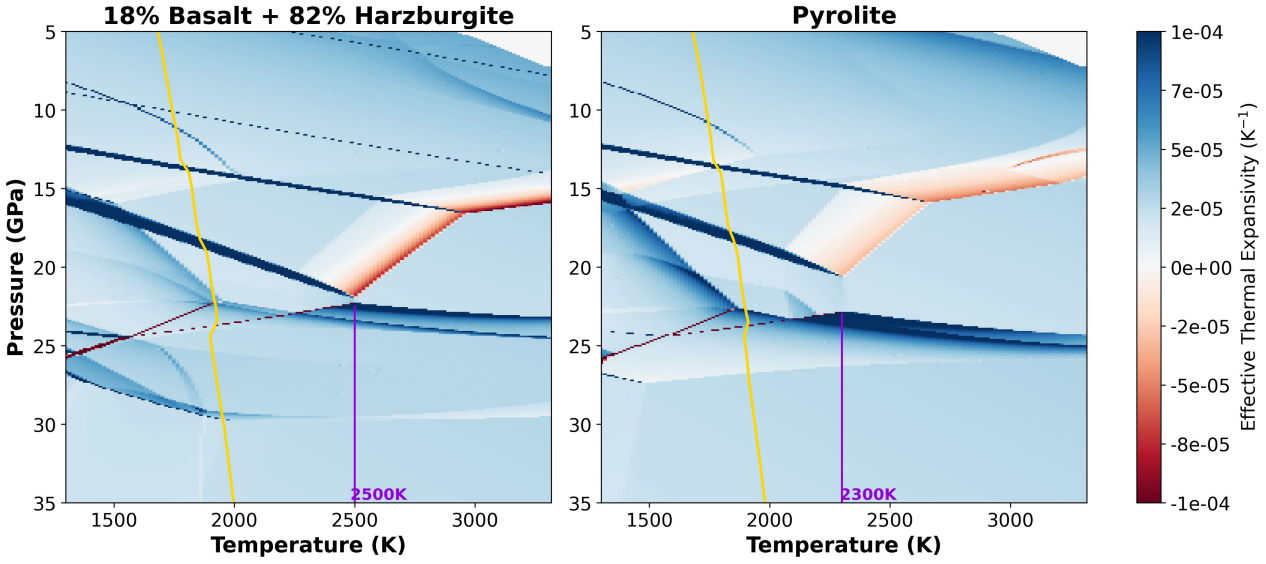

Figure 8. Effective thermal expansivity for a two-component basalt–harzburgite mixture with a pyrolitic bulk composition (left) and a single-component equilibrium pyrolitic mantle (right). Red areas correspond to endothermic transitions, and blue areas correspond to exothermic transitions. The dashed rendering of some phase transitions reflects the limited resolution of the lookup table. The yellow line shows an adiabat with a potential temperature of 1600 K. The purple line marks the upper-temperature limit of the ringwoodite ↔ bridgmanite + ferropericlase transition, above which ringwoodite is no longer stable.

5 Application to mantle convection

To demonstrate the applicability of our method to mantle convection models, we present two sets of models with different rheologies that highlight the importance of incorporating realistic equations of state and phase transitions of chemically heterogeneous mantle components. All models presented in this section adopt material property lookup tables based on the dataset of Stixrude and Lithgow-Bertelloni (2022). In both model series, the bulk chemical composition is the same, but they are treated differently. We compare: (1) a single-component system with an equilibrium pyrolitic assemblage and (2) a two-component system with a mechanical mixture of basalt and harzburgite. These systems exhibit distinct phase transition characteristics (Figure 8), with phase transformations spanning different P–T ranges. In particular, the ringwoodite ↔ bridgmanite + ferropericlase transition in the mechanical mixture extends to temperatures about 200 K higher than in the equilibrium pyrolite. While the one-component pyrolite model can be computed using our original entropy formulation (Dannberg et al., 2022; Li et al., 2025), the new multi-component approach enables models using mechanical mixtures of varying compositional fractions. Since the temperatures of different components are not identical at the same pressure–entropy conditions, their lookup tables cannot be directly averaged in pressure–entropy space. Consequently, thermal equilibration as described in Section 3.2 is necessary. The model results in the following sections show that even small differences in phase transitions between these two assemblages can lead to markedly different convective layering and mantle dynamics.

https://doi.org/10.5194/egusphere-2026-1972
Preprint. Discussion started: 14 April 2026
© Author(s) 2026. CC BY 4.0 License.

5.1 Purely viscous models

In our first set of models, both the single-component and the two-component model follow the spherical convection setup described in Dannberg et al. (2022), Section 3.3. They have a spherical annulus domain with an inner radius of 3481 km and an outer radius of 6371 km. The bulk entropy of the outer boundary is fixed to 656.462 J/K/kg, corresponding to a temperature of 300 K at surface. The bulk entropy of the inner boundary is fixed to 3021.448 J/K/kg, corresponding to a temperature of 4000 K at the core-mantle boundary. The rest of the domain initially follows an adiabatic profile with an entropy of 2535.08 J/K/kg (corresponding to a potential temperature of 1600 K). The viscosity is temperature-dependent, but has a constant value of 10^{21} Pa s along this adiabat. We refer the reader to Dannberg et al. (2022) for a detailed description of all other model characteristics.

Because the rheology only depends on temperature, hot thermal instabilities develop much more readily than cold downwellings. As a result, the models develop multiple rising plumes, while cold downwellings are less frequent and relatively weak. This imbalance leads to gradual heating over time. As a result, this setup is useful to investigate how the phase transitions of the two different mineral assemblages affect plume morphology, but it does not represent Earth-like convection.

In the two-component model (Figure 9, top panel), plumes are hindered more strongly by the ringwoodite to bridgmanite + ferropericlase transition at 660 km depth than for the pyrolite assemblage (bottom panel). This is particularly evident early in the simulation (Figure 9, first column). In the mechanical mixture model, many plume heads stall at 660 km depth. The density distribution (second row and top inset) shows that plume heads undergo a sharp density increase at this transition, making them negatively buoyant relative to the surrounding mantle. Consequently, their ascent is slowed or halted, and they spread laterally. While the pyrolite model also shows a clear density increase in the plume heads at 660 km depth, the magnitude of the density variation is smaller than in the two-component model (compare the insets). In addition to expanding laterally, the plumes continue to rise to shallower depths. By 175 Myr (second column), the mechanical mixture model has formed a high-temperature layer spawning secondary plumes that persists throughout the rest of the model evolution. This layer is less distinct in the pyrolite model. By 300 Myr (third column) significant stalled material remains in the mechanical mixture model, while little to no stalled plume material remains in the pyrolite model.

The differences in the evolution of plume layering between the two models is clearly visualized by plotting the laterally averaged entropy as a function of the model runtime (Figure 10). The accumulation of hot, high entropy material (red colors) in the mid-mantle illustrates a more pronounced stalling effect for the mechanical mixture (upper panel) that also persists longer. While plume layering occurs in the single-component model as well, it is significantly weaker and fades to almost nothing after 300 Myr.

Since all other model parameters are identical, the different plume behaviors in the two models must be caused by differences in phase transition characteristics. In the pyrolite table, the endothermic transition from ringwoodite to bridgmanite and ferropericlase does not extend to temperatures much higher than the 1600 K adiabat (Figure 8), and therefore can only impede plumes with excess temperatures less than 150–200 K. In the mechanical mixture, this transition extends to temperatures up to 200 K higher, and can therefore hinder most of the plumes, including the hot plumes rising in the early stages of the model.

https://doi.org/10.5194/egusphere-2026-1972
Preprint. Discussion started: 14 April 2026
© Author(s) 2026. CC BY 4.0 License.

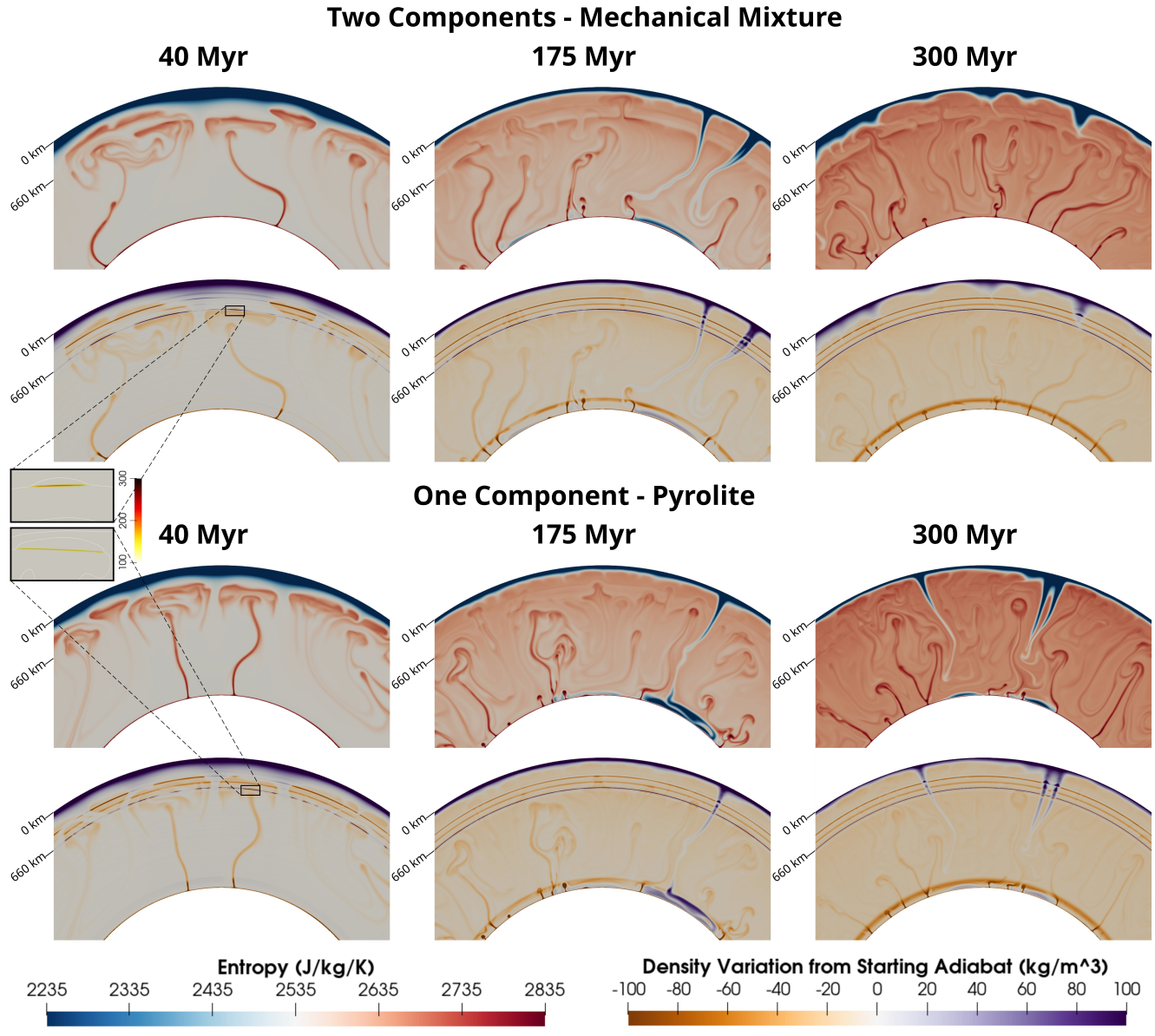

Figure 9. Snapshots of models with purely viscous rheology. The entropy field is shown in blue-to–red colors (blue indicates cold material), while density deviations from the starting adiabat are shown in purple–brown (purple indicates denser material). The top panel shows a model with two components, while the bottom panel shows a model with a single component but the same bulk composition. The thin density anomalies at approximately 410 km, 520km, and 660 km depth are caused by thermal conduction across the steep temperature gradient at these phase transitions leading to deviations from the initial density profile along the adiabat. The insets zoom in on the plume density anomalies and use a different color scale to highlight the differences between the two models. The white lines in the insets represent temperature contours that are 100 K hotter than the adiabatic temperature. In the two-component model, plumes are hindered more strongly at 660 km depth compared to the one-component model.

https://doi.org/10.5194/egusphere-2026-1972
Preprint. Discussion started: 14 April 2026
© Author(s) 2026. CC BY 4.0 License.

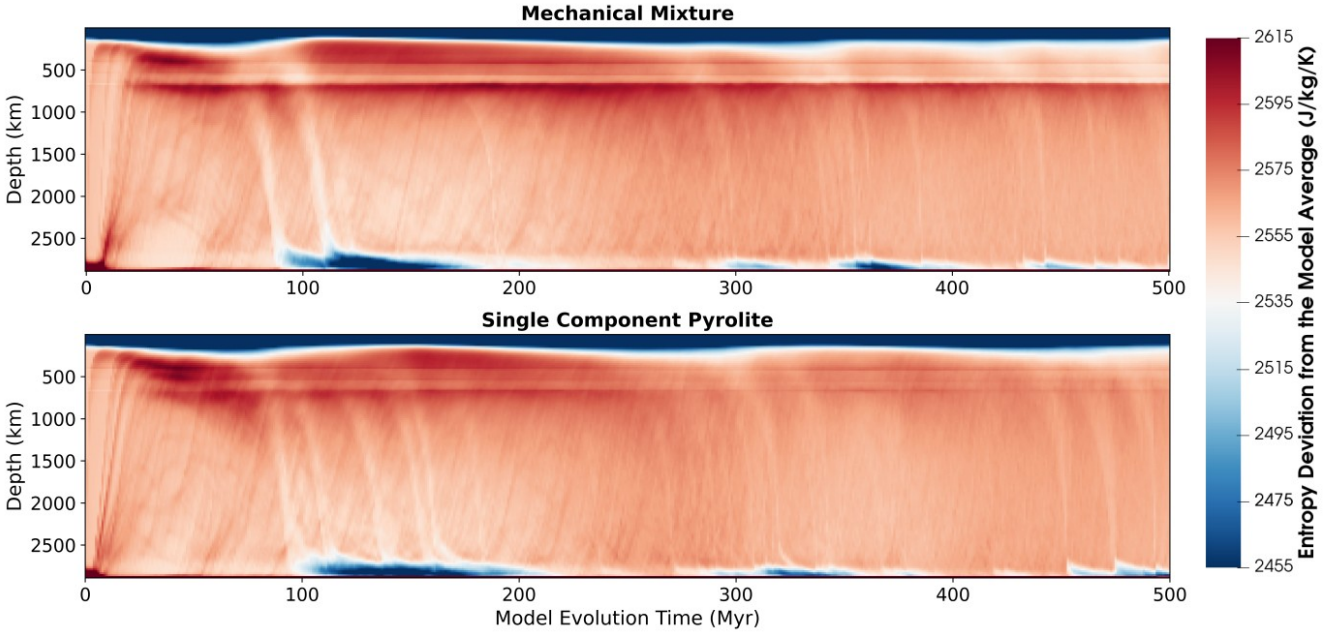

Figure 10. Deviation of the laterally averaged entropy from the average entropy of the whole model domain, plotted over the model evolution time for the purely viscous models. Since the average entropy changes, the thermal features are better illustrated by plotting the deviation from the current model average instead of the initial adiabat. Thin downward-sloping blue regions indicate cold downwellings (low entropy). Thin upward-sloping red streaks indicate rising plumes (high entropy). In addition to the accumulation of hot plume material at the base of the lithosphere, a second hot layer develops at approximately 660 km depth in both models.

5.2 Visco-plastic models

The second set of application models follows the setup of the more Earth-like spherical convection "Model 1600-4000" described in Li et al. (2025). They feature a more realistic rheology compared to the models in the previous section, including a depth-dependent reference viscosity profile with a strong increase in the lower mantle and a decrease in the asthenosphere (Steinberger and Calderwood, 2006), and plastic yielding in addition to the temperature-dependence. The single-component pyrolite model is identical to "Model 1600-4000" from Li et al. (2025), except that its material property lookup table is computed using the dataset of Stixrude and Lithgow-Bertelloni (2022) instead of Stixrude and Lithgow-Bertelloni (2011). The two-component models use the same mechanical mixture as discussed in Section 5.1.

Compared to the purely viscous models with only temperature-dependent viscosity, plumes in the second set of models rise from the core-mantle boundary less frequently but are hotter and larger in volume. As a result, they are less affected by the ringwoodite to bridgmanite + ferropericlase transition at 660 km, and no systematic plume layering occurs.

As in many previous studies, incorporating plastic yielding promotes plate-like behavior with subducting slabs. This has been demonstrated in models with single-component entropy advection (Li et al., 2025), and also holds for multi-component

https://doi.org/10.5194/egusphere-2026-1972
Preprint. Discussion started: 14 April 2026
© Author(s) 2026. CC BY 4.0 License.

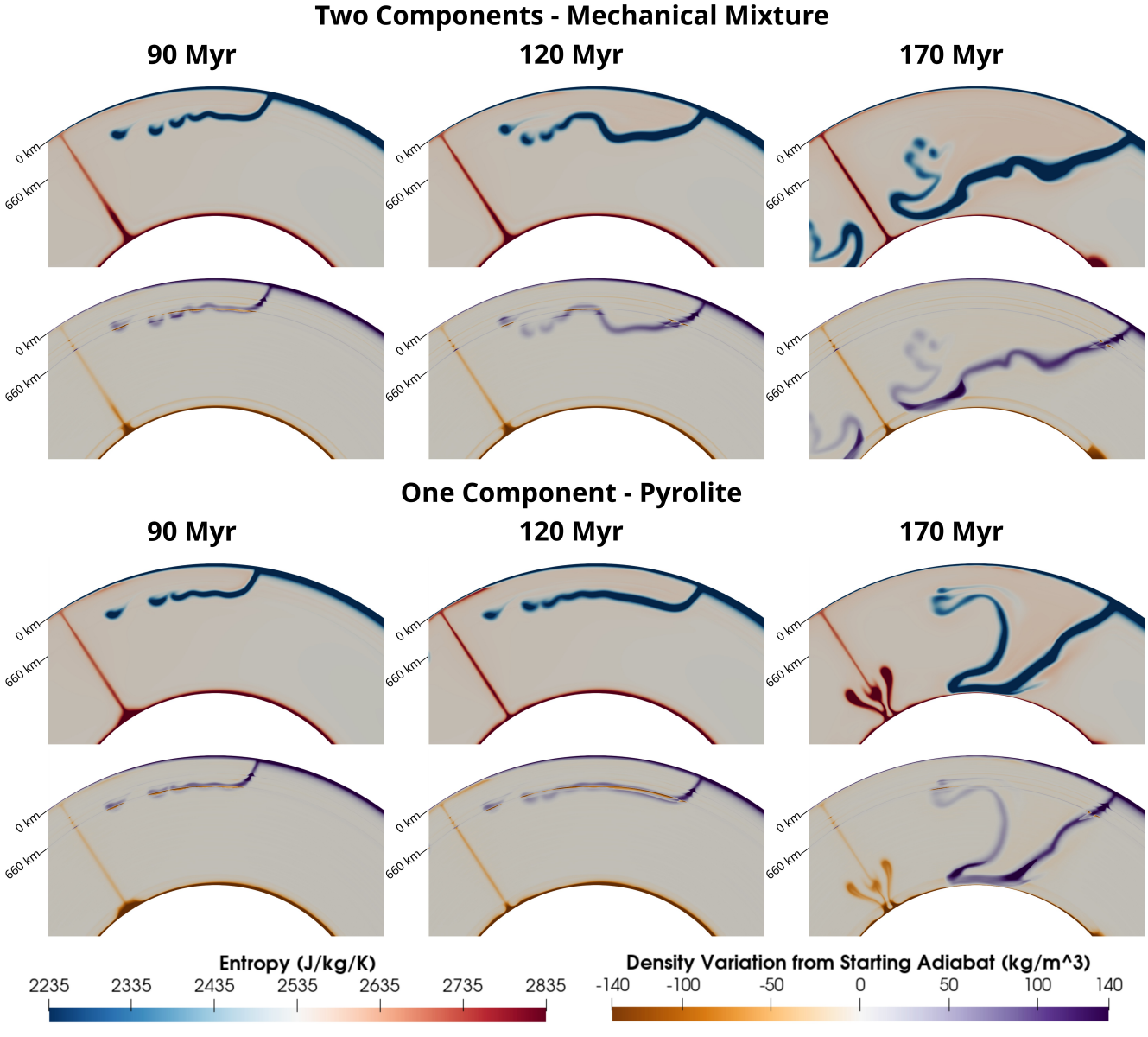

Figure 11. Snapshots of models with visco-plastic rheology. The figure layout and colors are as in Figure 9, except for the density deviation panels using a larger range for the colorbar. Subducting slabs are stalled at 660 km depth in both models, but for slightly different durations.

https://doi.org/10.5194/egusphere-2026-1972
Preprint. Discussion started: 14 April 2026
© Author(s) 2026. CC BY 4.0 License.

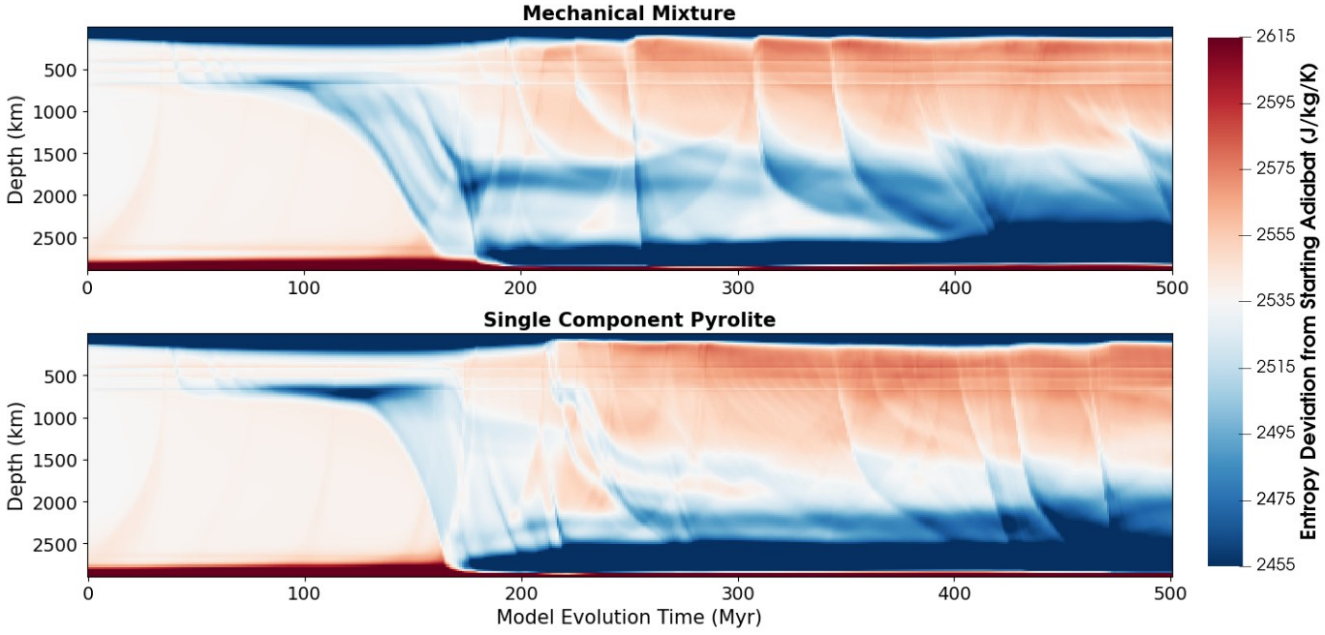

Figure 12. Deviation of laterally averaged entropy from the starting adiabat in the visco-plastic models, plotted over model evolution time with the same color scale as in Figure 10. Due to the plastic rheology, downwellings are stronger compared to the viscous models, forming plate-like subduction. The blue areas around 660 km depth indicate slab stagnation caused by the ringwoodite ↔ bridgmanite + ferropericlase phase transition.

entropy advection (Figure 11). The models therefore exhibit frequent downwellings, which are significantly affected by the 660 km phase transition. A comparison of the first slab in the mechanical mixture and pyrolite model (top and bottom panels of Figure 11) shows transient slab flattening at 660 km depth in both cases. The stagnation persists longer in the pyrolite model and is followed by a rapid slab avalanche (second and third column, bottom panel of Figure 11). This effect is also evident in the long-term thermal evolution (Figure 12). The pyrolite model (bottom panel) exhibits stronger slab stagnation during the first 150 Myr, as shown by the accumulation of cold downwellings (dark blue colors) around 660 km depth. Moreover, transient slab stagnation occurs as late as 230 Myr, whereas in the mechanical-mixture model, all slabs subducting after 200 Myr penetrate into the lower mantle without stalling. We note that slab stagnation results from the combined effects of the phase transition and the viscosity increase at 660 km depth. Since both models use the same viscosity profile, the contrasting slab behaviors must arise from differences in the equation of state between pyrolite and the mechanical mixture. The high thermal expansivity at 24–28 GPa and 1300–1900 K in the mechanical-mixture model (blue colors in Figure 8) strongly increases the density of the lower portion of the stalling slabs relative to those in the pyrolite model, leading to an increased negative buoyancy of slabs, which promotes faster sinking and earlier penetration into the lower mantle.

The example applications above demonstrate that even small variations in phase transitions can lead to substantial differences mantle convection style, affecting both rising plumes and subducted slabs.

https://doi.org/10.5194/egusphere-2026-1972
Preprint. Discussion started: 14 April 2026
© Author(s) 2026. CC BY 4.0 License.

6 Conclusions

We present a geodynamic modeling method that accurately captures the dynamic and latent heat effects of phase transitions in a heterogeneous mantle, even for complex phase relations and sharp transitions. We overcome the associated numerical challenges by extending our previous approach (Dannberg et al., 2022)—solving the energy equation for entropy rather than temperature—to incorporate multiple chemical components. This requires solving one entropy advection equation per component and a subsequent thermal equilibration that ensures that all components have the same temperature and that total entropy is conserved. Through a series of test cases, we demonstrate that our method is thermodynamically consistent, correctly computes the temperature and volume changes associated with different heating and heat transport mechanisms, conserves internal energy, and robustly handles even degenerate cases where multiple components undergo the same univariant phase transition.

We highlight the applicability of our method using two series of mantle convection models with different phase assemblages: a two-component basalt–harzburgite mixture, which requires our new approach, and a single-component pyrolite composition. The two assemblages feature different temperature ranges and material properties of the ringwoodite $\leftrightarrow$ bridgmanite + ferropericlase transition, which has a major impact on model evolution and leads to notable differences in plume and slab morphology. The extent of the ringwoodite $\leftrightarrow$ bridgmanite + ferropericlase transition to higher temperatures in the mechanical mixture causes a larger fraction of plumes to stagnate, while in the pyrolitic model subducted slabs stall at the boundary for longer periods due to their lower bulk density. Our results illustrate that even small differences in phase transitions can produce marked differences in convective layering and mantle dynamics.

We have implemented our method in the open-source geodynamic modeling software ASPECT, providing a flexible tool for the community to investigate the formation, evolution, and dynamic effects of mantle heterogeneity associated with phase transitions. Our method opens up a significant number of new applications for mantle convection models, including basalt segregation from subducted slabs, the ascent of thermo-chemical plumes, and the long-term thermo-chemical evolution of planetary mantles.

Code and data availability. The software, code modifications, input parameters, data, and log files used for the models in the study are available on Zenodo at DOI 10.5281/zenodo.18504402 under the MIT license (Li et al., 2026). ASPECT version 3.1.0-pre (commit hash 14e30a472), (Heister et al., 2017; Kronbichler et al., 2012; Bangerth et al., 2024a, b; Clevenger and Heister, 2021; Gassmöller et al., 2020; Dannberg et al., 2022) used in these computations can be found in our Zenodo data repository, and it is also freely available under the GPL v2.0 or later license through its software landing page and is being actively developed on GitHub. BurnMan and corresponding scripts are available in the linked data publication and also on GitHub.

Appendix A: Construction of lookup tables

In this section, we document the parameters, mineral physics databases, and smoothing procedures used to generate the lookup tables employed in the benchmark and application sections. For the benchmarks, we created nine different lookup tables in

https://doi.org/10.5194/egusphere-2026-1972
Preprint. Discussion started: 14 April 2026
© Author(s) 2026. CC BY 4.0 License.

BurnMan, as listed in Table A1, and for the application models we created three additional tables using PerpleX (Connolly, 2009). All lookup tables except for Table 6 are generated using the mineral physics database Stixrude and Lithgow-Bertelloni (2022). Table 6 is generated with Stixrude and Lithgow-Bertelloni (2011).

Lookup tables 1 and 2 are computed for a single pure mineral (Forsterite in Table 1, Enstatite in Table 2) each, with no phase transitions throughout the P–S range that is covered. Pressure ranges from 0 GPa to 50 GPa and entropy ranges from 626.49 J/K/kg to 3009.38 J/K/kg (corresponding to a temperature range from 301.018 K to 2221.38 K at 0 GPa). The table has 1001 points in entropy space and 51 points in pressure space, resulting in an entropy resolution of 23.83 J/K/kg and pressure resolution of 1 GPa. No smoothing is applied.

Lookup table 3 contains a phase change from pure Fo to Wad. We compute the stability fields of Fo and Wad, as well as their mixed region where the phase transition occurs. The table has 97 points in entropy space with a grid spacing of 5.73 J/K/kg, and 97 points in pressure space with a grid spacing of 0.0417 GPa. The enthalpy H on the P–S grid is smoothed with a 2-d Gaussian filter (sigma = 1 grid spacing) to obtain finite values for T, ρ, and effective C_P (see equation in Section 3.3). Pressure ranges from 11.5 GPa to 15.5 GPa and entropy ranges from 2056.23 J/K/kg to 2606.49 J/K/kg (corresponding to a temperature range from 1166.225 K to 1806.22 K at 11.5 GPa).

Lookup table 4 contains an artificial Fo to Wad phase change which is repositioned to intersect a 0 GPa isobar at 1200 K. To shift the Fo to Wad phase transition from its original pressure to this new position, we subtract a constant value from the Gibbs free energy of Wad so that it intersects with Fo at 0 GPa. We generated 101 points in pressure space ranging from -0.4 GPa to 0.4 GPa with a grid spacing of 0.008 GPa, and 1001 points in entropy space with a grid spacing of 2.01 J/K/kg. The entropy corresponds to a temperature range from 400 K to 2000 K at -0.8 GPa and 408.33 K to 1983.15 K at 0 GPa. We then apply the same Gaussian smoothing procedure as described for generating Lookup table 3, and with a σ of 2 grid spacings. After smoothing, we only keep the three pressure rows -0.008 GPa, 0 GPa, and 0.008 GPa, and discard the rest for computational efficiency.

Lookup table 5 contains a phase change from pure Fo to Wad. It has a finer resolution in entropy space (1001 points, equivalent to a 1.95 J/K/kg grid spacing) than Lookup table 3. Its pressure resolution is the same as in Lookup table 4, but pressure instead ranges from 12.6 GPa to 13.4 GPa. As for Lookup table 3, this table is smoothed using a Gaussian filter, with a σ of 2.5 grid spacings. After smoothing, we we only keep the three pressure grids -12.992 GPa, 13.0 GPa, and 13.008 GPa, and discard the rest for computational efficiency.

Lookup table 6 contains pure Forsterite, as in Lookup table 1, but has a higher entropy resolution of 1.96 J/K/kg to match the resolution of Tables 4 and 5 for Test 7b. The entropy space ranges from 901.16 J/K/kg to 2863.89 J/K/kg, corresponding to a temperature range from 400 K to 2000 K at 0 GPa. The table contains two pressure values: 0 GPa and 13 GPa. No smoothing is applied.

Lookup tables 7, 8, and 9 are generated using mineral physics data from Stixrude and Lithgow-Bertelloni (2011). These tables contains two mineral phases, Qtz and En, which do not react with each other. Qtz undergoes a phase transition to Coe. The procedure for generating the tables is the same as for Table 3, except that we compute the stability fields for the Qtz+En and Coe+En assemblages. All three tables have 131 points in both pressure and entropy space, with pressure ranging from

https://doi.org/10.5194/egusphere-2026-1972
Preprint. Discussion started: 14 April 2026
© Author(s) 2026. CC BY 4.0 License.

Table A1. Tables used in benchmark section

Test	Lookup table
1	Lookup table 1: Pure Fo
2	Lookup table 2: Pure En
3	
4a	
4b	
4c	Lookup table 1: Pure Fo Lookup table 3: Fo to Wad
5	Lookup table 1: Pure Fo
6	Lookup table 2: Pure En
7a	
7b	Lookup table 4: Fo to Wad (0 Gpa) Lookup table 5: Fo to Wad (13 GPa) Lookup table 6: Pure Fo (high resolution)
8	Lookup table 7: Qtz to Coe (40%) + En (60%) Lookup table 8: Qtz to Coe (60%) + En (40%) Lookup table 9: Qtz to Coe (54%) + En (46%)

1.13 GPa to 2.87 GPa with a grid spacing of 0.0133 GPa. They are all smoothed with σ of 1 grid spacing. Lookup table 7 contains 40% Qtz/Coesite and 60% En, and the entropy ranges from 1757.81 J/K/kg to 2207.82 J/K/kg with a grid spacing of 3.46 J/K/kg. Lookup table 8 contains 60% Qtz/Coesite and 40% En. The entropy space ranges from 1419.60 J/K/kg to 1785.76 J/K/kg with a grid spacing of 2.82 J/K/kg. Lookup table 9 contains 54% Qtz/Coesite and 46% En. The entropy space ranges from 1521.06 J/K/kg to 1912.38 J/K/kg with a grid spacing of 3.01 J/K/kg.

Application models: Pyrolite, basalt, and harzburgite lookup tables are generated using PerpleX and the mineral physics database Stixrude and Lithgow-Bertelloni (2022). The rock compositions follow Xu et al. (2008). In all three tables, pressure ranges from 0 GPa to 150 GPa with 1497 points in pressure direction and a grid spacing of 0.1 GPa. For the pyrolite table, entropy ranges from 387.28 J/K/kg to 3317.55 J/K/kg, corresponding to a temperature range from 209 K to 2868 K at 0 GPa. For the basalt table, entropy ranges from 365.64 J/K/kg to 3216.99 J/K/kg, corresponding to a temperature range from 208.74 K to 2831.4 K at 0 GPa. For the harzburgite table, entropy ranges from 395.23 J/K/kg to 3327.12 J/K/kg, corresponding to a temperature range from 209.95 K to 2876.31 K at 0 GPa.

All tables use 300 points in entropy direction, resulting in an entropy resolution of 9.8 J/K/kg for pyrolite, 9.5 J/K/kg for basalt, and 9.8 J/K/kg for harzburgite.

https://doi.org/10.5194/egusphere-2026-1972
Preprint. Discussion started: 14 April 2026
© Author(s) 2026. CC BY 4.0 License.

Appendix B: Logic of the thermal equilibration iterative scheme

At constant pressure, entropy and temperature are related by the expression

$$S(T_1) = S(T_0) + \int_{T_0}^{T_1} \frac{C_P(T)}{T}\, dT \tag{B1}$$

Since the equation of state is complicated, we evaluate this relation numerically. Assuming that C_P is constant with respect to T (i.e. $(\partial S/\partial \ln T)_P$ is constant), the relationship between temperature and entropy change over a iteration for a single composition i can be written

$$S_i^{[1]} = S_i^{[0]} + C_{Pi}^{[0]} \left(\ln T^{[1]} - \ln T_i^{[0]} \right). \tag{B2}$$

In a multicomponent material, we make the approximation that entropy is conserved during reaction. Although this is not exactly how reactions take place in the Earth, this is the same approximation that is made implicitly in simulations that combine different compositions / assemblages into a single lookup table. The requirement that total entropy is conserved during reaction can be written

$$\Delta S^{[1]-[0]} = 0 = \sum_i X_i \left(S_i^{[1]} - S_i^{[0]} \right) = \sum_i X_i C_{Pi}^{[0]} \left(\ln T^{[1]} 1_i - \ln T_i^{[0]} \right). \tag{B3}$$

This equation can be rearranged to find the temperature $T^{[1]}$ that satisfies entropy conservation, by splitting the sum on the RHS into two separate sums:

$$\sum_k X_k C_{Pk}^{[0]} \ln T^{[1]} 1_k = \sum_j X_j C_{Pj}^{[0]} \ln T_j^{[0]} \tag{B4}$$

$$\ln T^{[1]} = \frac{\sum_j X_j C_{Pj}^{[0]} \ln T_j^{[0]}}{\sum_k X_k C_{Pk}^{[0]}}. \tag{B5}$$

This temperature can now be used to estimate $S_i^{[1]}$ from Eq (B2), and lookup $T_i^{[1]}$ and $C_{Pi}^{[1]}$ for each component i for use in the next iteration.

Author contributions. RL, RG, JD, and RM jointly developed the concept of the study and the algorithm. RM developed the thermodynamical methodology and provided the mineral physics data, RL developed the necessary software components with review and supervision from RG, JD, and RM. RL performed the benchmark and application models, prepared the visualizations and wrote the original draft. RG, JD, RM jointly reviewed and edited the draft.

Competing interests. The authors have no competing interests to declare.

https://doi.org/10.5194/egusphere-2026-1972
Preprint. Discussion started: 14 April 2026
© Author(s) 2026. CC BY 4.0 License.

Acknowledgements. The authors acknowledge support by HELMHOLTZ funding of first-time professorial appointments of excellent women scientists to JD (EBP-01-08). ASPECT and BurnMan are hosted by the Computational Infrastructure for Geodynamics (CIG) which is supported by National Science Foundation Awards EAR 1550901 and 2149126. Open Access funding enabled and organized by Projekt DEAL.

https://doi.org/10.5194/egusphere-2026-1972
Preprint. Discussion started: 14 April 2026
© Author(s) 2026. CC BY 4.0 License.

References

Agrusta, R., van Hunen, J., and Goes, S.: Strong plates enhance mantle mixing in early Earth, Nature Communications, 9, 2708, 2018.

Arredondo, K. M. and Billen, M. I.: Coupled effects of phase transitions and rheology in 2-D dynamical models of subduction, Journal of Geophysical Research: Solid Earth, 122, 5813–5830, 2017.

Bangerth, W., Dannberg, J., Fraters, M., Gassmoeller, R., Glerum, A., Heister, T., Myhill, R., and Naliboff, J.: ASPECT v3.0.0, https://doi.org/10.5281/zenodo.14371679, 2024a.

Bangerth, W., Dannberg, J., Fraters, M., Gassmoeller, R., Glerum, A., Heister, T., Myhill, R., and Naliboff, J.: ASPECT: Advanced Solver for Planetary Evolution, Convection, and Tectonics, User Manual, https://doi.org/10.6084/m9.figshare.4865333, 2024b.

Billen, M. I.: Modeling the dynamics of subducting slabs, Annu. Rev. Earth Planet. Sci., 36, 325–356, 2008.

Christensen, U. R. and Yuen, D. A.: Layered convection induced by phase transitions, Journal of Geophysical Research: Solid Earth, 90, 10 291–10 300, 1985.

Clevenger, T. C. and Heister, T.: Comparison Between Algebraic and Matrix-free Geometric Multigrid for a Stokes Problem on an Adaptive Mesh with Variable Viscosity, Numerical Linear Algebra with Applications, https://doi.org/10.1002/nla.2375, 2021.

Connolly, J.: The geodynamic equation of state: what and how, Geochemistry, geophysics, geosystems, 10, 2009.

Cottaar, S., Heister, T., Rose, I., and Unterborn, C.: BurnMan: A lower mantle mineral physics toolkit, Geochemistry, Geophysics, Geosystems, 15, 1164–1179, 2014.

Dannberg, J. and Sobolev, S. V.: Low-buoyancy thermochemical plumes resolve controversy of classical mantle plume concept, Nature communications, 6, 6960, 2015.

Dannberg, J., Myhill, R., Gassmöller, R., and Cottaar, S.: The morphology, evolution and seismic visibility of partial melt at the core–mantle boundary: Implications for ULVZs, Geophysical Journal International, 227, 1028–1059, 2021.

Dannberg, J., Gassmöller, R., Li, R., Lithgow-Bertelloni, C., and Stixrude, L.: An entropy method for geodynamic modelling of phase transitions: capturing sharp and broad transitions in a multiphase assemblage, Geophysical Journal International, 231, 1833–1849, 2022.

Davaille, A., Le Bars, M., and Carbonne, C.: Thermal convection in a heterogeneous mantle, Comptes Rendus. Géoscience, 335, 141–156, 2003.

Dong, J., Fischer, R. A., Stixrude, L. P., Brennan, M. C., Daviau, K., Suer, T.-A., Turner, K. M., Meng, Y., and Prakapenka, V. B.: Nonlinearity of the post-spinel transition and its expression in slabs and plumes worldwide, Nature Communications, 16, 1039, 2025.

Faccenda, M. and Dal Zilio, L.: The role of solid–solid phase transitions in mantle convection, Lithos, 268, 198–224, 2017.

Fukao, Y. and Obayashi, M.: Subducted slabs stagnant above, penetrating through, and trapped below the 660 km discontinuity, Journal of Geophysical Research: Solid Earth, 118, 5920–5938, 2013.

Gassmöller, R., Dannberg, J., Bangerth, W., Heister, T., and Myhill, R.: On formulations of compressible mantle convection, Geophysical Journal International, 221, 1264–1280, 2020.

Gerya, T. V., Perchuk, L. L., Maresch, W. V., and Willner, A. P.: Inherent gravitational instability of hot continental crust: Implications for doming and diapirism in granulite facies terrains, in: Gneiss Domes in Orogeny, edited by Whitney, D. L., Teyssier, C., and Siddoway, C. S., p. 0, Geological Society of America, ISBN 9780813723808, https://doi.org/10.1130/0-8137-2380-9.97, 2004.

Goes, S., Yu, C., Ballmer, M. D., Yan, J., and van der Hilst, R. D.: Compositional heterogeneity in the mantle transition zone, Nature Reviews Earth & Environment, 3, 533–550, 2022.

https://doi.org/10.5194/egusphere-2026-1972
Preprint. Discussion started: 14 April 2026
© Author(s) 2026. CC BY 4.0 License.

Heister, T., Dannberg, J., Gassmöller, R., and Bangerth, W.: High Accuracy Mantle Convection Simulation through Modern Numerical Methods. II: Realistic Models and Problems, Geophysical Journal International, 210, 833–851, https://doi.org/10.1093/gji/ggx195, 2017.

Hirose, K., Fei, Y., Ma, Y., and Mao, H.-K.: The fate of subducted basaltic crust in the Earth's lower mantle, Nature, 397, 53–56, 1999.

Irifune, T. and Ringwood, A.: Phase transformations in subducted oceanic crust and buoyancy relationships at depths of 600–800 km in the mantle, Earth and Planetary Science Letters, 117, 101–110, 1993.

Jarvis, G. T. and McKenzie, D.: Convection in a compressible fluid with infinite Prandtl number, Journal of Fluid Mechanics, 96, 515–583, 1980.

Koppers, A. A., Becker, T. W., Jackson, M. G., Konrad, K., Müller, R. D., Romanowicz, B., Steinberger, B., and Whittaker, J. M.: Mantle plumes and their role in Earth processes, Nature Reviews Earth & Environment, 2, 382–401, 2021.

Kronbichler, M., Heister, T., and Bangerth, W.: High Accuracy Mantle Convection Simulation through Modern Numerical Methods, Geophysical Journal International, 191, 12–29, https://doi.org/10.1111/j.1365-246X.2012.05609.x, 2012.

Li, R., Dannberg, J., Gassmöller, R., Lithgow-Bertelloni, C., and Stixrude, L.: How phase transitions impact changes in mantle convection style throughout Earth's history: From stalled plumes to surface dynamics, Geochemistry, Geophysics, Geosystems, 26, e2024GC011 600, 2025.

Li, R., Dannberg, J., Gassmöller, R., and Myhill, R.: Modeling thermodynamically consistent phase transitions in multi-component assemblages: An entropy method for geodynamic models: Data and Software, https://doi.org/10.5281/zenodo.18504402, 2026.

Lin, S.-C. and van Keken, P. E.: Dynamics of thermochemical plumes: 1. Plume formation and entrainment of a dense layer, Geochemistry, Geophysics, Geosystems, 7, 2006.

McNamara, A. K. and Zhong, S.: Thermochemical structures within a spherical mantle: Superplumes or piles?, Journal of Geophysical Research: Solid Earth, 109, 2004.

Mulyukova, E., Steinberger, B., Dabrowski, M., and Sobolev, S. V.: Survival of LLSVPs for billions of years in a vigorously convecting mantle: Replenishment and destruction of chemical anomaly, Journal of Geophysical Research: Solid Earth, 120, 3824–3847, 2015.

Myhill, B., Heister, T., Cottaar, S., Rose, I., Unterborn, C., Esser, T., Gassmoeller, R., Knezek, N. R., Leinweber, K., Renaud, J., Farla, R., S-Hunt, and Bangerth, W.: geodynamics/burnman: BurnMan v2.1.0, https://doi.org/10.5281/zenodo.14238633, 2024.

Myhill, R., Cottaar, S., Heister, T., Rose, I., Unterborn, C., Dannberg, J., and Gassmoeller, R.: BurnMan–a Python toolkit for planetary geophysics, geochemistry and thermodynamics, Journal of Open Source Software, 8, 2023.

Nakagawa, T., Tackley, P. J., Deschamps, F., and Connolly, J. A.: Incorporating self-consistently calculated mineral physics into thermochemical mantle convection simulations in a 3-D spherical shell and its influence on seismic anomalies in Earth's mantle, Geochemistry, Geophysics, Geosystems, 10, 2009.

Nakagawa, T., Tackley, P. J., Deschamps, F., and Connolly, J. A.: The influence of MORB and harzburgite composition on thermo-chemical mantle convection in a 3-D spherical shell with self-consistently calculated mineral physics, Earth and Planetary Science Letters, 296, 403–412, 2010.

Peltier, W. and Solheim, L.: Mantle phase transitions and layered chaotic convection, Geophysical Research Letters, 19, 321–324, 1992.

Steinberger, B. and Calderwood, A. R.: Models of large-scale viscous flow in the Earth's mantle with constraints from mineral physics and surface observations, Geophysical Journal International, 167, 1461–1481, 2006.

Stixrude, L. and Lithgow-Bertelloni, C.: Thermodynamics of mantle minerals—I. Physical properties, Geophysical Journal International, 162, 610–632, 2005.

https://doi.org/10.5194/egusphere-2026-1972
Preprint. Discussion started: 14 April 2026
© Author(s) 2026. CC BY 4.0 License.

Stixrude, L. and Lithgow-Bertelloni, C.: Thermodynamics of mantle minerals-II. Phase equilibria, Geophysical Journal International, 184, 1180–1213, 2011.

Stixrude, L. and Lithgow-Bertelloni, C.: Thermal expansivity, heat capacity and bulk modulus of the mantle, Geophysical Journal International, 228, 1119–1149, 2022.

Tackley, P. J.: On the penetration of an endothermic phase transition by upwellings and downwellings, Journal of Geophysical Research: Solid Earth, 100, 15 477–15 488, 1995.

Torsvik, T. H., Smethurst, M. A., Burke, K., and Steinberger, B.: Large igneous provinces generated from the margins of the large low-velocity provinces in the deep mantle, Geophysical Journal International, 167, 1447–1460, 2006.

Xu, W., Lithgow-Bertelloni, C., Stixrude, L., and Ritsema, J.: The effect of bulk composition and temperature on mantle seismic structure, Earth and Planetary Science Letters, 275, 70–79, 2008.

Yan, J., Ballmer, M. D., and Tackley, P. J.: The evolution and distribution of recycled oceanic crust in the Earth's mantle: Insight from geodynamic models, Earth and Planetary Science Letters, 537, 116 171, 2020.